Structural cohesive element for the modelling of delamination in composite laminates without the cohesive zone limit

Ai, Xiaopeng; Chen, Boyang; Kassapoglou, Christos

DOI
10.1016/j.engfracmech.2025.111586

Publication date
2025

Document Version
Final published version

Published in
Engineering Fracture Mechanics

Citation (APA)
Ai, X., Chen, B., & Kassapoglou, C. (2025). Structural cohesive element for the modelling of delamination in composite laminates without the cohesive zone limit. *Engineering Fracture Mechanics*, *329*, Article 111586. https://doi.org/10.1016/j.engfracmech.2025.111586

Engineering Fracture Mechanics 329 (2025) 111586

Contents lists available at ScienceDirect

Engineering Fracture Mechanics

journal homepage: www.elsevier.com/locate/engfracmech

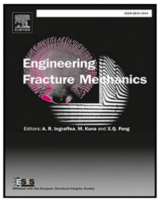

Structural cohesive element for the modelling of delamination in composite laminates without the cohesive zone limit

Xiaopeng Ai, Boyang Chen *, Christos Kassapoglou

Department of Aerospace Structures and Materials, Faculty of Aerospace Engineering, Delft University of Technology, Kluyverweg 1, Delft, 2629 HS, The Netherlands

ARTICLE INFO

Keywords:
Composites
Delamination
Cohesive zone model
Cohesive element

ABSTRACT

Delamination is a critical mode of failure that occurs between plies in a composite laminate. The cohesive element, developed based on the cohesive zone model, is widely used for modelling delamination. However, standard cohesive elements suffer from a well-known limit on the mesh density—the element size must be much smaller than the cohesive zone size. This work extends the line of research on *structural* cohesive elements onto 3D mixed-mode problems. A new triangular Kirchhoff–Love shell element is developed for orthotropic materials to model the plies. A new *structural* cohesive element, conforming to the shell elements of the plies, is developed to model the interface delamination. The proposed method is verified and validated on the classical benchmark problems of Mode I, Mode II, and mixed-mode delamination of unidirectional laminates, a recent unidirectional benchmark problem with curved delamination front, as well as the single-leg bending problem of a multi-directional laminate, significantly increasing the range and complexity of applicable problems as compared to the previous works. All the results show that the element size in the proposed models can be ten times larger than that in the standard cohesive element models, with more than 90% reduction in CPU time, while retaining prediction accuracy. This would then allow more effective and efficient modelling of delamination in composites without worrying about the cohesive zone limit on the mesh density.

1. Introduction

The accurate prediction of delamination is of critical importance for the reliable design of fibre-reinforced composite structures. The cohesive element (CE) is a widely used finite element technology to model delamination. CE is developed based on the Cohesive Zone Model proposed by Dugdale and Barenblatt [1,2]. A fracture process zone, generally called the cohesive zone, exists along the interface, ahead of the stress-free crack tip. A traction–separation relationship, namely the cohesive law, describes how the interfacial stresses and damage evolve with respect to the interfacial openings. Standard CEs are usually developed for use between two solid elements to model their debonding under static or fatigue loads [3–12]. In finite element implementation, cohesive zone models are classified into intrinsic and extrinsic types. In the intrinsic model, CEs are embedded in the initial mesh between continuum elements to model their debonding. Intrinsic CEs firstly undergo an elastic loading phase, up to the critical stress state for damage onset, before going through the softening phase of the cohesive law. In the extrinsic model, CEs are inserted/activated in the mesh on the fly when the stress state in the continuum has reached damage onset. Hence, extrinsic CEs only go through the softening phase of the cohesive law. Comprehensive comparisons of the two approaches have been performed for dynamic fracture problems [13–15]. Intrinsic CEs are easy to implement and parallelize, but suffer from the artificial compliance problems in crack-tip speed and

---

* Corresponding author.
E-mail address: b.chen-2@tudelft.nl (B. Chen).

https://doi.org/10.1016/j.engfracmech.2025.111586
Received 23 May 2025; Received in revised form 22 September 2025; Accepted 26 September 2025

Nomenclature

Latin characters

a_0	Pre-crack length
A	Area of a membrane element
b	Width
$\mathbf{B}$	Matrix connecting the vector $\mathbf{Q}$ and the vector α
$\mathbf{B}_{\mathrm{mem}}$	Strain–displacement matrix of a membrane element
$\mathbf{D}_{\mathrm{mem}}$	Constitutive tensor of a membrane element
$E_{(ij)}$	Young's modulus($i = 1, 2, 3$ $j = 1, 2, 3$)
$\mathbf{f}_{\mathrm{ext}}$	Vector of the external force
$\mathbf{f}_{\mathrm{int}}$	Vector of the internal force
$\mathbf{f}_{\mathrm{res}}$	Vector of the residual force
G_{I}, G_{II}	Mode I, Mode II energy release rates
G_{Ic}, G_{IIc}	Mode I, Mode II critical energy release rates
$\mathbf{H}$	Matrix which contributes to the stiffness matrix of the plate element
$\mathbf{K}$	Stiffness matrix of a finite element
K	Penalty stiffness
l_{ij}	Length of the side ij, $ij = 12, 23, 13$
L	Length
M_n	Normal bending moment
$\mathbf{N}_w$	Shape function related to the out-of-plane displacement
$\mathbf{N}_{\theta_x}, \mathbf{N}_{\theta_y}$	Shape function related to the rotations around x and y, respectively
$p^*(x, y)$	Prescribed distributed pressure load on the element
$\mathbf{q}$	Vector of nodal degree of freedoms of a finite element
$\mathbf{Q}$	Vector of generalized forces
R_N	Concentrated force at the element vertex
t	Thickness of a element
$\mathbf{T}$	Matrix contributes the stiffness matrix of the plate element
u_i, v_i	Displacements along x and y axes for node i
$\overline{\mathbf{U}}$	Vector of nodal degree of freedoms of the membrane element
U	Internal work
U_0	Strain energy density
V_n	Kirchhoff shear force
w	Displacement field in the element
$\overline{w}$	Displacement on the boundary of the element
$\overline{\mathbf{W}}$	Vector of nodal degree of freedoms of the plate element
W	External work

Greek characters

α	Vector of coefficients that contributes to the out-of-plane displacement field
γ	Angle between the normal n and the local axis x
$\Delta_{\mathrm{I}}, \Delta_x, \Delta_y$	Opening displacement of Mode I and two shear openings along x and y axial
π	Modified potential energy

Sub/superscripts

$\bullet_{\mathrm{mem}}$	Related to membrane elements
$\bullet_{\mathrm{plate}}$	Related to plate elements
$\bullet_{\mathrm{shell}}$	Related to shell elements
$\bullet_{\mathrm{bot}}$	Related to the bot surface of a cohesive element
$\bullet_{\mathrm{CE}}$	Related to cohesive elements
$\bullet_n$	Related to the normal direction
$\bullet_x, \bullet_y$	Related to the global x, y directions, respectively

Abbreviations

CE	Cohesive Element
CZL	Cohesive Zone Length
DCB	Double Cantilever Beam
DoF	Degrees of Freedom
ENF	End-Notched-Flexure
FE	Finite Element
FNM	Floating Node Method
IG	InteGration points
MMB	Mixed-Mode Bending
R-DCB	Reinforced Double Cantilever Beam
SLB	Single-Leg Bending
VCCT	Virtual Crack Closure Technique

elastic wave propagation [15]. High penalty stiffness is needed to reduce the artificial compliance problems, but this would lead to ill-conditioning of the stiffness matrix for implicit analysis and stringent stability requirements for explicit analysis. Extrinsic CEs do not add artificial compliance before fracture. However, their implementation would require advanced data structures and frequent updates of the mesh [16], making implementation and parallelization more difficult. Discontinuous-Galerkin [17] and Augmented Lagrangian [18] approaches have been developed to mitigate the artificial compliance problems of the intrinsic CEs without requiring mesh updates of the extrinsic CEs. However, they still suffer from the mesh dependency problems due to the restriction that the cohesive fracture can only propagate along existing mesh boundaries. In this work, we focus on quasi-static analysis of delamination in composites. Hence, the artificial compliance issues in dynamic fracture are neglected and the intrinsic model is assumed for the CEs hereafter.

While being a popular and versatile tool to model delamination, standard CEs suffer from a well-known limit on the mesh density — the element size must be much smaller than the Cohesive Zone Length (CZL) to accurately predict delamination. According to the previous analysis [3,4], high-stress gradients could be produced within the cohesive zone during delamination in composites. A very fine CE mesh must be used there to sufficiently capture the stress gradients such that the internal virtual work of the CEs can be accurately integrated. So far, there is no fixed rule on how fine the mesh should be in the literature. In some research [5–7], the authors have demonstrated that at least two or three CEs should be used inside the cohesive zone. With coarser meshes, simulations would significantly over-predict the peak load [8]. In a typical mode I delamination test of a unidirectional composites coupon, i.e., the Double Cantilever Beam (DCB) test, the CZL is less than 1 mm.

The above-mentioned problem of cohesive zone limit on the mesh density of CEs has drawn the attention of many researchers in the past. Turon et al. [8] adopted an engineering method to solve the problem by reducing the material strength to numerically extend the CZL. While shown to be promising in the Mode I DCB case, in cases such as the pure mode II End-Notched-Flexure (ENF) test, decreasing the cohesive strength can cause excessive under-prediction of the overall strength [19,20]. Yang [21] and Do [22]'s research work demonstrated that larger CE sizes can be achieved by placing enough integration points in the cohesive zone. Their method could predict the peak load correctly for CE size up to 1.43 times the estimated CZL. However, its first-order shape function limits the effectiveness of this method in further expanding CE beyond the scale of the cohesive zone [23]. Guiamatsia et al. [24–26] used the beam on elastic foundation solution as an enrichment function and tested it in the mixed mode delamination. However, the enrichment method could lead to inaccuracies in interpolation for elements larger than 3 mm [25]. Another enrichment approach with the piecewise linear shape functions was proposed by Samimi [27–29]. However, the over-prediction problem of peak load under large CE has not been solved. Van der Meer et al. [30] used the level set method with a energy-based criterion to propagate delamination without the cohesive zone limit. However, this method is limited to the case of a single delamination. Lu et al. [31] proposed a adaptive version of the Floating Node Method (FNM) [32] to adaptively refine the CEs in the cohesive zone. However, this method is currently implemented for 2D problems. Alvarez et al. [33] used quadratic CEs between quadratic solid elements and used higher number of integration points, which increased the grid size to be comparable to CZL but not beyond [23]. Mukhopadhyay and Bhatia [34] developed a *hp* refinement strategy to simulate the delamination between two solid elements. However, it is only implemented in 2D in their work. Daniel [35] developed an ERR-Cohesive method to simulate the delamination with large elements by estimating the energy release rate by means of the virtual crack closure technique (VCCT). However, this method is only presented in 2D, and the VCCT approach relies on the existence of an initial crack and the assumption of self-similar crack propagation.

Inspired by the earlier works in the literature, Russo and Chen [23] developed a so-called structural CE, which conforms to Kirchhoff–Love structural elements for the neighbouring plies. Their work was done in 2D. The Euler–Bernoulli beam elements were used to model the plies. The structural CE, sharing its nodes with the beam elements, was developed to model the delamination. An adaptive integration scheme was used to place more integration points in CEs containing the cohesive zone. Their results showed that the structural CE could overcome the cohesive zone limit on mesh density, allowing the element size to be ten times larger than that of the standard linear CEs. Motivated by Russo and Chen's work, Tosti Balducci and Chen [36] extended the structural CE to 3D DCB problem by developing a structural CE compatible with the TUBA3 plate elements [37]. Their results showed that the TUBA3-based structural formulation of CE could overcome the cohesive zone limit. However, the curvature degrees of freedom (DoFs) make it complicated to set boundary conditions on TUBA3 elements, impeding the adoption of such elements by engineers in practice.

From the above reviews, we aim to establish a composites delamination model which simultaneously meets the following requirements:

(1) it does not suffer from the cohesive zone limit on mesh density;
(2) it works in 3D space;
(3) it does not require artificial reduction of strengths;
(4) it does not require a pre-crack and the self-similar propagation assumption;
(5) it can model delamination along multiple interfaces; and
(6) it is straightforward to set boundary conditions.

Based on the earlier works [23,36], the idea of this work is to develop a triangular Kirchhoff–Love shell element without curvature DoFs to model the composite plies, then formulate the conforming structural CE to be used between the plies to model their delamination. Although previous researchers [38,39]have used shell elements and the corresponding CEs to simulate delamination, their focus was mainly on the use of shell elements per se and did not solve the problem of cohesive zone limitations on mesh density. The shell element in this work is based on a simple triangle Kirchhoff–Love plate element, the cubic displacement element proposed by Allman [40]. There are only three DoFs at each node, one for out-of-plane displacement and two for rotations. These DoFs are commonly used by engineers and are much easier to handle than the curvature ones when setting boundary conditions. Therefore, this article will extend this triangle plate element for the modelling of composite plies and develop the corresponding structural CE for the interfaces. If such a structural CE could overcome the cohesive zone limit on its mesh density, then it would achieve all the requirements listed above. Although this paper addresses objectives similar to those of previous studies [23,36], it offers significant advantages over the preceding two works in the following aspects:

(1) The previous methods did not modify the underlying isotropic beam or plate element for the plies, limiting the scope of the modelling to isotropic beam or plate bending problems. In contrast, this study firstly enriches the baseline plate element to include in-plane degrees of freedom, thereby extending the plate element to a shell element. It then extends the supported material model from being isotropic to being suitable for composites. These developments are essential for the modelling of generic deformations of composite shell structures.
(2) The previous methods are applicable to 2D mixed-mode [23] or 3D mode-I [36] problems. This study extends the structural CE method to be applicable for 3D mixed-mode problems, thereby enabling the modelling of more general and more complex problems beyond the plane-strain delamination problems of the standard test coupons;
(3) The baseline plate element employed in this study features a reduced number of degrees of freedom compared to the TUBA3 element in the previous 3D work [36]. As a result, the implementation of the method is simpler and the application of boundary conditions more direct than in the case of the TUBA3 elements. These advantages will make simulations more efficient when dealing with large-scale and complex models with complex boundary conditions.
(4) Furthermore, this study verifies the method on fully 3D problems with complex stacking sequences and crack fronts. This is a significant improvement over the earlier work in terms of the complexity and scope of the verification.

The rest of the paper will be structured in the following way. Section 2 presents the proposed element formulations in detail. Section 3 demonstrates the performance of these elements on a series of benchmarks on delamination in both unidirectional and multi-directional laminates. In the end, Section 4 draws the conclusions of this work and discusses some potential future work.

2. Method

2.1. Overall illustration

The overall idea of the proposed modelling approach is to represent the composite plies by Kirchhoff–Love shell elements and the interfaces by structural CEs. Fig. 1 shows the geometrical comparison between the conventional modelling approach with solid elements and the proposed structural approach with shells. Looking at the structural CE, the difference from the conventional CE is that the nodes of the CE are placed at the mid-plane of the two shell elements, which are not the actual surfaces of the cohesive interface. Hence, the opening of the actual interface does not equate to the distance between the upper nodes and lower ones of the structural CE. This opening shall be calculated using the shell kinematics to be detailed in later subsections. The rest of this section will firstly present the cubic plate element formulation by Allman [40] and its adaptation for flat composites shells, then move on to derive the structural CE formulation.

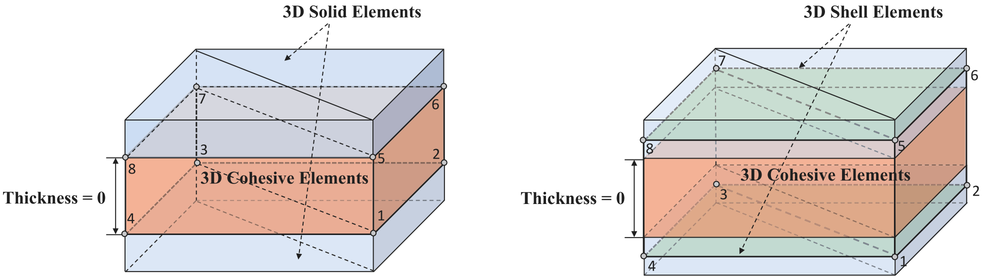

(a) Conventional CE between solids: interface thickness = distance between node 4 and node 8 (b) Structural CE between shells: interface thickness ≠ distance between node 4 and node 8

Fig. 1. Geometrical comparison between conventional CE and structural CE.

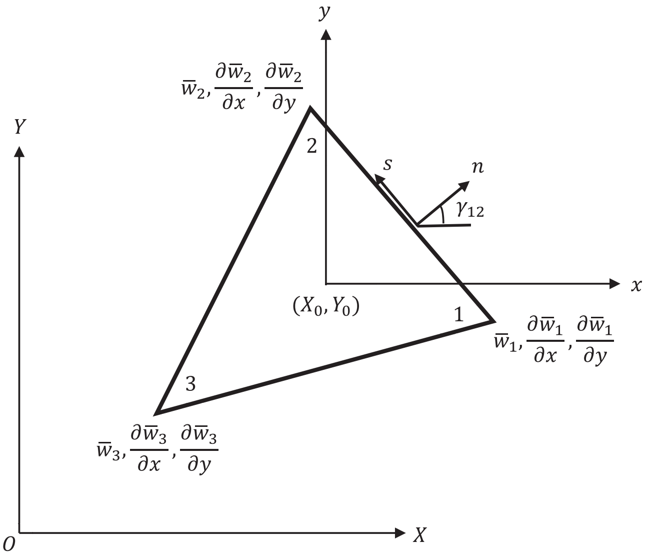

Fig. 2. Coordinate system and DoFs for the triangular cubic plate element [40].

2.2. Cubic plate element

2.2.1. Geometric definitions of the plate element

The plate part of the shell element in this work is based on the triangular cubic plate element developed by Allman [40], as shown in Fig. 2. A local coordinate system is used in this element, with origin at the centroid of the triangular element. The local axes are represented by lowercase letters, x and y, to distinguish them from the global ones, X and Y. The area of this triangular element is A. s is the anti-clockwise coordinate along the element boundary. n is the exterior normal. The angle between the normal n and the local axis x is γ. The out-of-plane displacement defined over the domain is $w(x, y)$. An independent out-of-plane boundary displacement, $\overline{w}(s)$, and its compatible normal derivative, $\partial\overline{w}/\partial n(s)$, are assumed along the boundary ∂A. The DoFs at each node include the displacement $\overline{w}$ and two rotations $\partial\overline{w}/\partial x$, $\partial\overline{w}/\partial y$.

The cubic plate element in Allman's work only considered the case of isotropic material [40]. This work extends the cubic plate element using the classical laminate theory, such that symmetric composite laminates can also be modelled by this plate element. The original cubic element formulation will be presented in detail, with adaptations for composites specified along the way.

2.2.2. Modified potential energy for the plate element

The minimum potential energy principle is used to derive the finite element formulation of the triangular plate element. The potential energy used is referred to as the modified potential energy in Allman's work [40]:

$$\pi = \iint_A U_0 \mathrm{d}x\mathrm{d}y + \sum_{N=1}^{3} R_N(\overline{w}_N - w_N) + \int_{\partial A} V_n(\overline{w} - w)\,\mathrm{d}s - \int_{\partial A} M_n(\frac{\partial \overline{w}}{\partial n} - \frac{\partial w}{\partial n})\mathrm{d}s$$

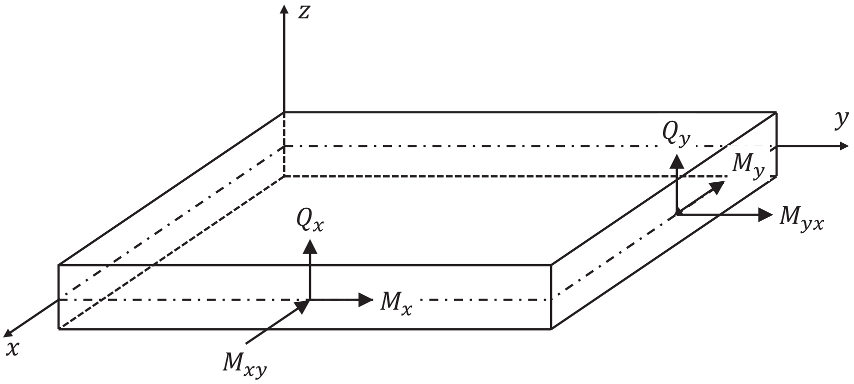

Fig. 3. Sign conventions for shear force and bending moment resultants.

$$-\iint_A p^* w \mathrm{d}x\mathrm{d}y - \sum_{N=1}^{3} R_N^* \overline{w}_N - \int_{\partial A} V_n^* \overline{w} \mathrm{d}s + \int_{\partial A} M_n^* \frac{\partial \overline{w}}{\partial n} \mathrm{d}s \tag{1}$$

where U_0 is the strain energy density. M_n is the normal bending moment resultant and V_n is the Kirchhoff shear force distribution on the element boundary, respectively. $R_{N\,(N=1,2,3)}$ are the concentrated forces at the element vertices. In addition, R_N^*, V_n^*, and M_n^* are the values of prescribed concentrated force, Kirchhoff shear force, and normal bending moment resultant, respectively. $p^*(x,y)$ denotes the prescribed distributed pressure load on the element. This potential energy essentially uses R_N, V_n, and M_n as Lagrange multipliers to enforce the compatibility between the two fields w and $\overline{w}$ and their normal derivatives along the boundary. The variational principle based on this modified potential energy satisfies the equilibrium equations, the boundary conditions, and the compatibility requirement between w and $\overline{w}$ [40].

The expression of U_0 for composites will be different from that for isotropic materials in Allman's work [40]. The classical laminate theory can be used to describe the constitutive relationship of a composite laminate under Kirchhoff–Love kinematic assumptions. For the case of a symmetric laminate (the smallest of which would be a single composite ply) considered in this work, there would be no membrane-bending coupling. Therefore, the expressions of the moments are:

$$\begin{aligned} M_x &= -D_{11}\frac{\partial^2 w}{\partial x^2} - D_{12}\frac{\partial^2 w}{\partial y^2} - 2D_{16}\frac{\partial^2 w}{\partial x \partial y} \\ M_y &= -D_{12}\frac{\partial^2 w}{\partial x^2} - D_{22}\frac{\partial^2 w}{\partial y^2} - 2D_{26}\frac{\partial^2 w}{\partial x \partial y} \\ M_{xy} &= -D_{16}\frac{\partial^2 w}{\partial x^2} - D_{26}\frac{\partial^2 w}{\partial y^2} - 2D_{66}\frac{\partial^2 w}{\partial x \partial y} \end{aligned} \tag{2}$$

Using the above moment–curvature relations (Eq. (2)), the strain energy density U_0 can be written as:

$$\begin{aligned} U_0 = \frac{1}{2}\Bigg[& D_{11}\left(\frac{\partial^2 w}{\partial x^2}\right)^2 + D_{22}\left(\frac{\partial^2 w}{\partial y^2}\right)^2 + 2D_{12}\frac{\partial^2 w}{\partial x^2}\frac{\partial^2 w}{\partial y^2} \\ & +4D_{16}\frac{\partial^2 w}{\partial x^2}\frac{\partial^2 w}{\partial x \partial y} + 4D_{26}\frac{\partial^2 w}{\partial y^2}\frac{\partial^2 w}{\partial x \partial y} + 4D_{66}\left(\frac{\partial^2 w}{\partial x \partial y}\right)^2 \Bigg] \end{aligned} \tag{3}$$

The sign conventions for the shear force and bending moment resultants are shown in Fig. 3. For the triangular plate element, the normal bending moment resultant M_n, Kirchhoff shear force distribution V_n and concentrated forces $R_{N\,(N=1,2,3)}$ can be expressed as [40]:

$$M_n = M_x \cos^2\gamma + M_y \sin^2\gamma + M_{xy}\sin 2\gamma \tag{4}$$

$$V_n = Q_n + \frac{\partial M_{ns}}{\partial s} \tag{5}$$

$$R_N = [M_{ns}]_{s^-}^{s^+} \tag{6}$$

where

$$M_{ns} = \frac{1}{2}(M_y - M_x)\sin 2\gamma + M_{xy}\cos 2\gamma \tag{7}$$

$$Q_n = \frac{\partial M_n}{\partial n} + \frac{\partial M_{ns}}{\partial s} \tag{8}$$

In this element, linear variation of the normal bending moment resultant and constant Kirchhoff shear force distribution are assumed along the edges:

$$M_n = M_n^{12}(1-\xi) + M_n^{21}\xi \tag{9}$$

$$V_n = V_n^{12} \tag{10}$$

where M_n^{12} and M_n^{21} are the normal bending moment resultant values at node 1 and node 2 of side 1-2 respectively. The coefficient ξ in Eq. (9) is defined as $\xi = s/l_{12}$. V_n^{12} is the value of the Kirchhoff shear force distribution along the side 1-2. The cyclic permutation of superscripts 1, 2, and 3 in Eqs. (9) and (10) produces the shear force distribution and moment resultant on the other two sides (side 2-3 and side 3-1) of the triangular element.

The terms in brackets in Eq. (6) represent the difference in bending moment resultant values at the element vertices. Therefore, the expressions of $R_{N\,(N=1,2,3)}$ are:

$$\begin{aligned} R_1 &= M_{ns}^{12} - M_{ns}^{13} \\ R_2 &= M_{ns}^{23} - M_{ns}^{21} \\ R_3 &= M_{ns}^{31} - M_{ns}^{32} \end{aligned} \tag{11}$$

Finally, the directional derivatives in Eqs. (8) are given by:

$$\begin{aligned} \frac{\partial}{\partial s} &= -\sin\gamma \frac{\partial}{\partial x} + \cos\gamma \frac{\partial}{\partial y} \\ \frac{\partial}{\partial n} &= \cos\gamma \frac{\partial}{\partial x} + \sin\gamma \frac{\partial}{\partial y} \end{aligned} \tag{12}$$

2.2.3. Finite element approximation and the discretized equilibrium equation

For finite element implementation, the potential energy π should be discretized. In this element, the internal out-of-plane displacement field $w(x,y)$ is approximated by a cubic polynomial:

$$w(x,y) = A_1 + A_2\,x + A_3\,y + \alpha_1\,x^2 + \alpha_2\,xy + \alpha_3\,y^2 + \alpha_4\,x^3 + \alpha_5\,x^2y + \alpha_6\,xy^2 + \alpha_7\,y^3 \tag{13}$$

The three coefficients A_1, A_2, and A_3 represent the rigid body motion and do not affect the value of the strain energy density.

With the above choice of w, applying the Green's theorem [41] to transform the strain energy integral to boundary integral gives:

$$2\iint_A U_0\,\mathrm{d}x\mathrm{d}y = \sum_{N=1}^{3} R_N w_N + \int_{\partial A} V_n w\,\mathrm{d}s - \int_{\partial A} M_n \frac{\partial w}{\partial n}\,\mathrm{d}s \tag{14}$$

In this work, we assume that there is no distributed pressure load $p^*(x,y)$. Then, the modified potential energy (Eq. (1)) can be rewritten more simply as:

$$\begin{aligned} \pi = &-\iint_A U_0\,\mathrm{d}x\mathrm{d}y + \sum_{N=1}^{3} R_N \overline{w}_N + \int_{\partial A} V_n \overline{w}\,\mathrm{d}s - \int_{\partial A} M_n \frac{\partial \overline{w}}{\partial n}\,\mathrm{d}s \\ &- \sum_{N=1}^{3} R_N^* \overline{w}_N - \int_{\partial A} V_n^* \overline{w}\,\mathrm{d}s + \int_{\partial A} M_n^* \frac{\partial \overline{w}}{\partial n}\,\mathrm{d}s \end{aligned} \tag{15}$$

Substituting Eq. (13) into (3), the strain energy can be rewritten as:

$$\iint_A U_0\,\mathrm{d}x\mathrm{d}y = \frac{1}{2}\boldsymbol{\alpha}^{\mathrm{T}}\,\mathbf{H}\,\boldsymbol{\alpha} \tag{16}$$

where the vector $\boldsymbol{\alpha}$ is:

$$\boldsymbol{\alpha} = \{\alpha_1, \alpha_2, \alpha_3, \alpha_4, \alpha_5, \alpha_6, \alpha_7\}^{\mathrm{T}} \tag{17}$$

The matrix $\mathbf{H}$ is more complicated to derive for symmetric composite laminates than for isotropic materials considered in Ref. [40]. Its detailed derivation is presented in Appendix A.

After the strain energy, the 2nd, 3rd and 4th terms in Eq. (15) denote the work of the so-called generalized forces:

$$\sum_{N=1}^{3} R_N \overline{w}_N + \int_{\partial A} V_n \overline{w}\,\mathrm{d}s - \int_{\partial A} M_n \frac{\partial \overline{w}}{\partial n}\,\mathrm{d}s = \mathbf{Q}^{\mathrm{T}}\mathbf{q} \tag{18}$$

where $\mathbf{Q}$ is the vector of the twelve generalized forces:

$$\mathbf{Q} = \{R_1, R_2, R_3, V_n^{12}, V_n^{23}, V_n^{31}, M_n^{12}, M_n^{21}, M_n^{23}, M_n^{32}, M_n^{31}, M_n^{13}\}^{\mathrm{T}} \tag{19}$$

Substituting Eqs. (9) and (10) into Eq. (18), the generalized displacements corresponding to the generalized forces in Eq. (19) compose the vector $\mathbf{q}$:

$$\begin{aligned} \mathbf{q} = \Bigg\{ &\overline{w}_1,\ \overline{w}_2,\ \overline{w}_3,\ l_{12}\int_0^1 \overline{w}\,\mathrm{d}\xi,\ l_{23}\int_0^1 \overline{w}\,\mathrm{d}\xi,\ l_{31}\int_0^1 \overline{w}\,\mathrm{d}\xi, \\ &-l_{12}\int_0^1 \frac{\partial \overline{w}}{\partial n}(1-\xi)\,\mathrm{d}\xi,\ -l_{12}\int_0^1 \frac{\partial \overline{w}}{\partial n}\xi\,\mathrm{d}\xi,\ -l_{23}\int_0^1 \frac{\partial \overline{w}}{\partial n}(1-\xi)\,\mathrm{d}\xi, \end{aligned}$$

$$-l_{23}\int_0^1 \frac{\partial \overline{w}}{\partial n}\xi\,\mathrm{d}\xi,\ -l_{31}\int_0^1 \frac{\partial \overline{w}}{\partial n}(1-\xi)\,\mathrm{d}\xi,\ -l_{31}\int_0^1 \frac{\partial \overline{w}}{\partial n}\xi\,\mathrm{d}\xi \Bigg\}^{\mathrm{T}} \tag{20}$$

A matrix $\mathbf{B}$ can be constructed to connect the vector $\mathbf{Q}$ and the vector $\boldsymbol{\alpha}$:

$$\mathbf{Q} = \mathbf{B}^{\mathrm{T}}\boldsymbol{\alpha} \tag{21}$$

With the moment–curvature relationship for composites in Eq. (2) and the expression of w in equation (13), the matrix $\mathbf{B}$ has been derived for composites in this work. The details are shown in Appendix B.

A matrix $\mathbf{T}$ can be defined to represent the relationship between the nodal DoFs $\overline{\mathbf{W}}$ and the vector $\mathbf{q}$:

$$\mathbf{q} = \mathbf{T}\overline{\mathbf{W}} \tag{22}$$

where $\overline{\mathbf{W}}$ is the vector of the nodal DoFs defined by

$$\overline{\mathbf{W}} = \left\{ \overline{w}_1, \frac{\partial \overline{w}_1}{\partial x}, \frac{\partial \overline{w}_1}{\partial y}, \overline{w}_2, \frac{\partial \overline{w}_2}{\partial x}, \frac{\partial \overline{w}_3}{\partial y}, \overline{w}_3, \frac{\partial \overline{w}_3}{\partial x}, \frac{\partial \overline{w}_3}{\partial y} \right\}^{\mathrm{T}} \tag{23}$$

With the assumptions of cubic line function for $\overline{w}$ and linear variation for $\partial \overline{w}/\partial n$ along each edge of the element, the $\mathbf{T}$ matrix can be derived as [40]:

$$\begin{bmatrix}
1 & 0 & 0 & 0 & 0 & 0 & 0 & 0 & 0 \\
0 & 0 & 0 & 1 & 0 & 0 & 0 & 0 & 0 \\
0 & 0 & 0 & 0 & 0 & 0 & 1 & 0 & 0 \\
\frac{l_{12}}{2} & -\frac{l_{12}^2}{12}\sin\gamma_{12} & \frac{l_{12}^2}{12}\cos\gamma_{12} & \frac{l_{12}}{2} & \frac{l_{12}^2}{12}\sin\gamma_{12} & -\frac{l_{12}^2}{12}\cos\gamma_{12} & 0 & 0 & 0 \\
0 & 0 & 0 & \frac{l_{23}}{2} & -\frac{l_{23}^2}{12}\sin\gamma_{23} & \frac{l_{23}^2}{12}\cos\gamma_{23} & \frac{l_{23}}{2} & \frac{l_{23}^2}{12}\sin\gamma_{23} & -\frac{l_{23}^2}{12}\cos\gamma_{23} \\
\frac{l_{31}}{2} & \frac{l_{31}^2}{12}\sin\gamma_{31} & -\frac{l_{31}^2}{12}\cos\gamma_{31} & 0 & 0 & 0 & \frac{l_{31}}{2} & -\frac{l_{31}^2}{12}\sin\gamma_{31} & \frac{l_{31}^2}{12}\cos\gamma_{31} \\
0 & -\frac{l_{12}}{3}\cos\gamma_{12} & -\frac{l_{12}}{3}\sin\gamma_{12} & 0 & -\frac{l_{12}}{6}\cos\gamma_{12} & -\frac{l_{12}}{6}\sin\gamma_{12} & 0 & 0 & 0 \\
0 & -\frac{l_{12}}{6}\cos\gamma_{12} & -\frac{l_{12}}{6}\sin\gamma_{12} & 0 & -\frac{l_{12}}{3}\cos\gamma_{12} & -\frac{l_{12}}{3}\sin\gamma_{12} & 0 & 0 & 0 \\
0 & 0 & 0 & 0 & -\frac{l_{23}}{3}\cos\gamma_{23} & -\frac{l_{23}}{3}\sin\gamma_{23} & 0 & -\frac{l_{23}}{6}\cos\gamma_{23} & -\frac{l_{23}}{6}\sin\gamma_{23} \\
0 & 0 & 0 & 0 & -\frac{l_{23}}{6}\cos\gamma_{23} & -\frac{l_{23}}{6}\sin\gamma_{23} & 0 & -\frac{l_{23}}{3}\cos\gamma_{23} & -\frac{l_{23}}{3}\sin\gamma_{23} \\
0 & -\frac{l_{31}}{6}\cos\gamma_{31} & -\frac{l_{31}}{6}\sin\gamma_{31} & 0 & 0 & 0 & 0 & -\frac{l_{31}}{3}\cos\gamma_{31} & -\frac{l_{31}}{3}\sin\gamma_{31} \\
0 & -\frac{l_{31}}{3}\cos\gamma_{31} & -\frac{l_{31}}{3}\sin\gamma_{31} & 0 & 0 & 0 & 0 & -\frac{l_{31}}{6}\cos\gamma_{31} & -\frac{l_{31}}{6}\sin\gamma_{31}
\end{bmatrix} \tag{24}$$

2.2.4. *Stiffness matrix and force vectors of cubic plate element*

Substituting Eqs. (16), (21) and (22) into Eq. (15), the total modified potential energy represented by the finite element method under prescribed boundary loads is:

$$\pi = -\frac{1}{2}\boldsymbol{\alpha}^{\mathrm{T}}\mathbf{H}\boldsymbol{\alpha} + \boldsymbol{\alpha}^{\mathrm{T}}(\mathbf{BT})\overline{\mathbf{W}} - \mathbf{Q}^{*\mathrm{T}}\mathbf{T}\overline{\mathbf{W}} \tag{25}$$

where the vector $\mathbf{Q}^*$, whose components are obtained by replacing the generalized forces in vector $\mathbf{Q}$ with the corresponding prescribed quantities, denotes all the external forces:

$$\mathbf{Q}^* = \{R_1^*, R_2^*, R_3^*, V_n^{*12}, V_n^{*23}, V_n^{*31}, M_n^{*12}, M_n^{*21}, M_n^{*23}, M_n^{*32}, M_n^{*31}, M_n^{*13}\}^{\mathrm{T}} \tag{26}$$

Thus, the internal work U and the external work W of the potential energy can be expressed as:

$$U = -\frac{1}{2}\boldsymbol{\alpha}^{\mathrm{T}}\mathbf{H}\boldsymbol{\alpha} + \boldsymbol{\alpha}^{\mathrm{T}}(\mathbf{BT})\overline{\mathbf{W}} \tag{27}$$

$$W = \mathbf{Q}^{*\mathrm{T}}\mathbf{T}\overline{\mathbf{W}} \tag{28}$$

Based on Eq. (25), the minimum total potential energy principle gives:

$$\delta\pi = \delta\boldsymbol{\alpha}^{\mathrm{T}}[(\mathbf{BT})\overline{\mathbf{W}} - \mathbf{H}\boldsymbol{\alpha}] + \delta\overline{\mathbf{W}}^{\mathrm{T}}[(\mathbf{BT})^{\mathrm{T}}\boldsymbol{\alpha} - \mathbf{T}^{\mathrm{T}}\mathbf{Q}^*] = 0 \tag{29}$$

Setting the coefficient of the arbitrary variation $\delta\boldsymbol{\alpha}^{\mathrm{T}}$ to zero gives:

$$\boldsymbol{\alpha} = \mathbf{H}^{-1}(\mathbf{BT})\overline{\mathbf{W}} \tag{30}$$

Performing the variation of U as expressed in (27) with $\boldsymbol{\alpha}$ substituted by Eq. (30), we arrive at δU for the element as:

$$\delta U = \delta\overline{\mathbf{W}}^{\mathrm{T}}(\mathbf{BT})^{\mathrm{T}}\mathbf{H}^{-1}(\mathbf{BT})\overline{\mathbf{W}} = \delta\overline{\mathbf{W}}^{\mathrm{T}}\mathbf{f}_{\mathrm{int}} \tag{31}$$

where $\mathbf{f}_{\mathrm{int}}$ is the internal force vector of the plate element:

$$\mathbf{f}_{\mathrm{int}} = (\mathbf{BT})^{\mathrm{T}}\mathbf{H}^{-1}(\mathbf{BT})\,\overline{\mathbf{W}} = \mathbf{K}_{\mathrm{plate}}\,\overline{\mathbf{W}} \tag{32}$$

and $\mathbf{K}_{\mathrm{plate}}$ is the stiffness matrix of the plate element:

$$\mathbf{K}_{\mathrm{plate}} = (\mathbf{BT})^{\mathrm{T}}\mathbf{H}^{-1}(\mathbf{BT}) \tag{33}$$

The variation of the external work W gives the external force vector of the element in the absence of distributed pressure load:

$$\delta W = \delta \overline{\mathbf{W}}\,\mathbf{T}^{\mathrm{T}}\mathbf{Q}^{*} = \delta \overline{\mathbf{W}}\,\mathbf{f}_{\mathrm{ext}}, \quad \Rightarrow \quad \mathbf{f}_{\mathrm{ext}} = \mathbf{T}^{\mathrm{T}}\mathbf{Q}^{*} \tag{34}$$

2.3. *Formation of shell element*

To form a flat shell element that considers membrane deformation and bending, we superimpose a linear membrane element on top of the plate element developed in the previous section. The displacement fields u, v are defined in terms of area coordinates L_1, L_2, L_3:

$$u = u_1 L_1 + u_2 L_2 + u_3 L_3 \tag{35}$$

$$v = v_1 L_1 + v_2 L_2 + v_3 L_3 \tag{36}$$

where u_i and v_i represent the displacements along x and y for node i, respectively. The DoFs vector of the membrane element $\overline{\mathbf{U}}$ is:

$$\overline{\mathbf{U}} = \left\{u_1,\, v_1,\, u_2,\, v_2,\, u_3,\, v_3\right\}^{\mathrm{T}} \tag{37}$$

The stiffness matrix of the triangular membrane element is given by the expression:

$$\mathbf{K}_{\mathrm{mem}} = \iint_{\Delta} \mathbf{B}_{\mathrm{mem}}^{\mathrm{T}}\,\mathbf{D}_{\mathrm{mem}}\,\mathbf{B}_{\mathrm{mem}}\, t\,\mathrm{d}x\,\mathrm{d}y \tag{38}$$

where t is the thickness of the membrane element and $\mathbf{B}_{\mathrm{mem}}$ matrix in Eq. (38) is

$$\mathbf{B}_{\mathrm{mem}} = \frac{1}{2A}\begin{bmatrix} b_1 & 0 & b_2 & 0 & b_3 & 0 \\ 0 & c_1 & 0 & c_2 & 0 & c_3 \\ c_1 & b_1 & c_2 & b_2 & c_3 & b_3 \end{bmatrix} \tag{39}$$

A is the area of the membrane element and:

$$b_1 = y_2 - y_3, \quad b_2 = y_3 - y_1, \quad b_3 = y_1 - y_2 \tag{40}$$

$$c_1 = x_3 - x_2, \quad c_2 = x_1 - x_3, \quad c_3 = x_2 - x_1 \tag{41}$$

The $\mathbf{D}^{\mathrm{mem}}$ matrix in Eq. (38) is:

$$\mathbf{D}_{\mathrm{mem}} = \begin{bmatrix} \frac{E_1}{1-\nu_{12}\nu_{21}} & \frac{\nu_{12}E_2}{1-\nu_{12}\nu_{21}} & 0 \\ & \frac{E_2}{1-\nu_{12}\nu_{21}} & 0 \\ \text{symmetric} & & G_{12} \end{bmatrix} \tag{42}$$

From Eqs. (33) and (38), we have obtained the stiffness matrices of the plate and membrane elements, respectively. They are assembled to form the stiffness matrix of the shell element:

$$\mathbf{K}_{\mathrm{shell}} = \begin{bmatrix} \mathbf{K}_{\mathrm{mem}} & 0 \\ 0 & \mathbf{K}_{\mathrm{plate}} \end{bmatrix} \tag{43}$$

The corresponding DoF vector of the shell element is simply:

$$\begin{aligned} \mathbf{q}_{\mathrm{shell}} &= \left\{\overline{\mathbf{U}}, \overline{\mathbf{W}}\right\} \\ &= \left\{u_1, v_1, u_2, v_2, u_3, v_3, w_1, \frac{\partial \overline{w}_1}{\partial x}, \frac{\partial \overline{w}_1}{\partial y}, \overline{w}_2, \frac{\partial \overline{w}_2}{\partial x}, \frac{\partial \overline{w}_3}{\partial y}, \overline{w}_3, \frac{\partial \overline{w}_3}{\partial x}, \frac{\partial \overline{w}_3}{\partial y}\right\}^{\mathrm{T}} \end{aligned} \tag{44}$$

The contribution of the shell element to the overall force residual of the finite element system equation is $\mathbf{f}_{\mathrm{ext}} - \mathbf{f}_{\mathrm{int}}$. When the applied loads are nodal forces, $\mathbf{f}_{\mathrm{ext}}$ does not need to be calculated explicitly in the element subroutine as the nodal forces can be directly entered in the global external force vector of the system. In this case, the residual contribution of this element can be expressed as:

$$\mathbf{f}_{\mathrm{res}} = -\mathbf{f}_{\mathrm{int}} = -\mathbf{K}_{\mathrm{shell}}\,\mathbf{q}_{\mathrm{shell}} \tag{45}$$

2.4. *Structural CE between two plies*

2.4.1. *DoFs and opening vector*

The structural CEs must be compatible with the top and bottom shell elements kinematically. Thus, they need to share the same DoFs and displacement interpolations along the interface. The DoF vector of the CE can be defined as:

$$\mathbf{q}_{\mathrm{CE}} = \left[\overline{\mathbf{U}}_{\mathrm{bot}}^{\mathrm{T}}, \overline{\mathbf{W}}_{\mathrm{bot}}^{\mathrm{T}}, \overline{\mathbf{U}}_{\mathrm{top}}^{\mathrm{T}}, \overline{\mathbf{W}}_{\mathrm{top}}^{\mathrm{T}}\right]^{\mathrm{T}} \tag{46}$$

where $\overline{\mathbf{U}}_{\mathrm{bot/top}}, \overline{\mathbf{W}}_{\mathrm{bot/top}}$ are the membrane and plate DoFs of the bottom/top ply, respectively.

The Mode I opening displacement of the CE can be expressed as

$$\Delta_{\mathrm{I}} = w^{\mathrm{topCE}} - w^{\mathrm{botCE}} \tag{47}$$

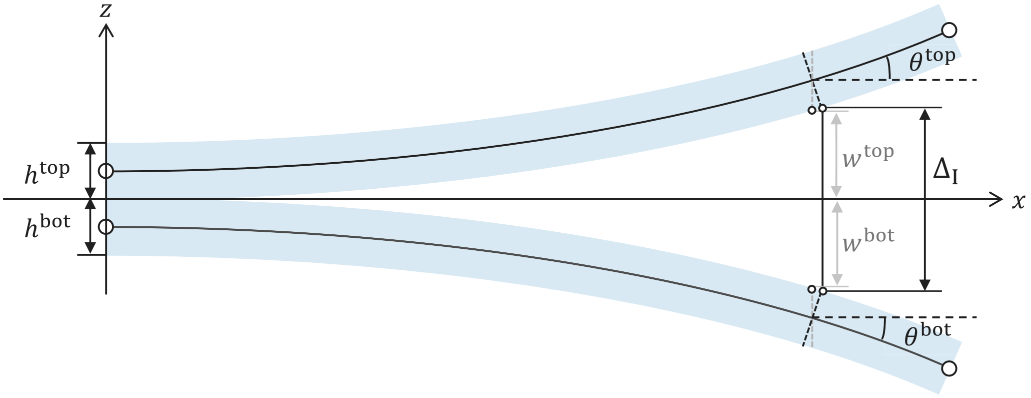

Fig. 4. Mode I opening.

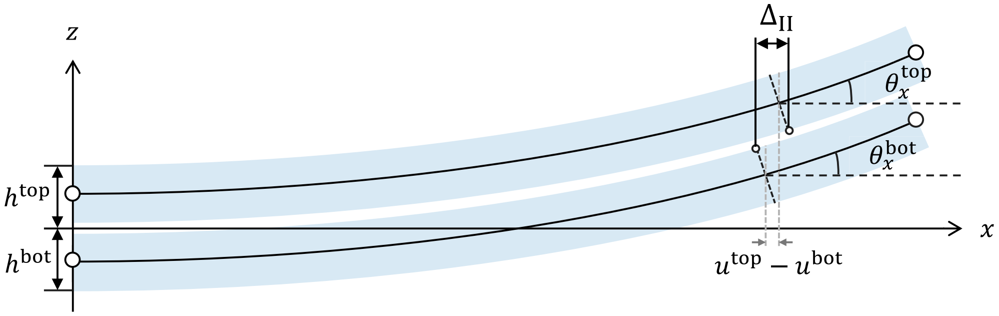

Fig. 5. Mode II opening.

where w^{topCE} and w^{botCE} are the vertical displacements of the top and bottom CE surfaces, respectively. From Fig. 4, using classical plate theory, we have:

$$w^{\text{topCE}} = w^{\text{top}} + \frac{h^{\text{top}}}{2}(1 - \cos\theta^{\text{top}}) \tag{48}$$

$$w^{\text{botCE}} = w^{\text{bot}} - \frac{h^{\text{bot}}}{2}(1 - \cos\theta^{\text{bot}}) \tag{49}$$

h^{top} and h^{bot} are the thickness of top and bottom plies, respectively. w^{top} and w^{bot} are the vertical displacements of the neutral planes of top and bottom plies, respectively. In this work, only geometrical linearity is considered. Thus, the rotations are small such that $1 - \cos\theta \approx 0$. The mode I opening is then simply the relative displacement between the mid-planes of the plies:

$$\Delta_{\text{I}} = w^{\text{top}} - w^{\text{bot}} \tag{50}$$

The Mode II opening of the CE shown in Fig. 5 can be expressed as:

$$\Delta_x = u^{\text{topCE}} - u^{\text{botCE}} \tag{51}$$

where u^{topCE} and u^{botCE} are the displacements along the x-axis of the top and bottom CE surfaces, respectively. Considering the rotations of the shells' neutral planes and the offsets of shell surfaces from the neutral planes, they can be written as:

$$u^{\text{topCE}} = u^{\text{top}} + \frac{h^{\text{top}}}{2}\sin\theta_x^{\text{top}} \tag{52}$$

$$u^{\text{botCE}} = u^{\text{bot}} - \frac{h^{\text{bot}}}{2}\sin\theta_x^{\text{bot}} \tag{53}$$

where u^{top}, u^{bot} are the displacement u of the neutral planes of the top and bottom shells, respectively. For a small rotation θ in geometrically linear problems, $\sin\theta \approx \theta$. Then, the shear opening along x is:

$$\Delta_x = u^{\text{top}} - u^{\text{bot}} + \frac{h^{\text{top}}}{2}\theta_x^{\text{top}} + \frac{h^{\text{bot}}}{2}\theta_x^{\text{bot}} \tag{54}$$

The shear opening along y is found from analogous kinematics in the yz-plane. Hence:

$$\Delta_y = v^{\text{top}} - v^{\text{bot}} + \frac{h^{\text{top}}}{2}\theta_y^{\text{top}} + \frac{h^{\text{bot}}}{2}\theta_y^{\text{bot}} \tag{55}$$

The central task of CE formulation is to find the matrix, $\mathbf{B}_{\mathrm{CE}}$, that relates the opening vector to its nodal DoFs:

$$\boldsymbol{\Delta} = \left[\Delta_{\mathrm{I}}, \Delta_x, \Delta_y\right]^{\mathrm{T}} = \mathbf{B}_{\mathrm{CE}}\, \mathbf{q}_{\mathrm{CE}} \tag{56}$$

Examining the expressions of $\Delta_{\mathrm{I}}, \Delta_{\mathrm{II}}, \Delta_{\mathrm{III}}$ in Eqs. (50), (54), and (55), we can see that the $\mathbf{B}_{\mathrm{CE}}$ matrix shall be composed of sub-matrices that relate the following terms to the nodal DoFs in $\mathbf{q}_{\mathrm{CE}}$:

$$w^{\mathrm{top}},\ w^{\mathrm{bot}},\ u^{\mathrm{top}},\ u^{\mathrm{bot}},\ v^{\mathrm{top}},\ v^{\mathrm{bot}},\ \theta_x^{\mathrm{top}},\ \theta_x^{\mathrm{bot}},\ \theta_y^{\mathrm{top}},\ \theta_y^{\mathrm{bot}} \tag{57}$$

In Eq. (35), the in-plane displacements u and v are already expressed in the nodal membrane DoFs. However, the out-of-plane displacements w and the rotations θ in the above list remain to be explicitly expressed in terms of nodal DoFs in $\mathbf{q}_{\mathrm{CE}}$.

2.4.2. Shape functions of w

The displacement w shall be expressed in terms of plate DoFs $\overline{\mathbf{W}}$ in this section. Referring back to Eq. (13), the displacement w is defined in the local Cartesian coordinates (x and y) by the coefficients A_i and the vector $\boldsymbol{\alpha}$. The expression of w is then divided into two parts. The first part only contains A_i, and the second part only contains α_j:

$$w = w_A + w_\alpha \tag{58}$$

where

$$w_A = A_1 + A_2\, x + A_3\, y \tag{59}$$

$$w_\alpha = \alpha_1\, x^2 + \alpha_2\, xy + \alpha_3\, y^2 + \alpha_4\, x^3 + \alpha_5\, x^2 y + \alpha_6\, xy^2 + \alpha_7\, y^3 \tag{60}$$

w_A can be rewritten as:

$$w_A = \mathbf{S}^{\mathrm{T}}\, \mathbf{A}, \quad \mathbf{S} = [1,\ x,\ y]^{\mathrm{T}},\ \mathbf{A} = [A_1,\ A_2,\ A_3]^{\mathrm{T}} \tag{61}$$

Similarly, w_α can be rewritten as:

$$w_\alpha = \mathbf{R}^{\mathrm{T}}\, \boldsymbol{\alpha}, \quad \mathbf{R} = [x^2,\ xy,\ y^2,\ x^3,\ x^2 y,\ xy^2,\ y^3]^{\mathrm{T}} \tag{62}$$

Let us firstly look at w_α. Based on Eq. (30), $\boldsymbol{\alpha}$ and $\overline{\mathbf{W}}$ can be related by multiplying the three matrices $\mathbf{H}$, $\mathbf{B}$ and $\mathbf{T}$ in Section 2.2.4. Here, for simplicity, we replace the product of these three matrices with matrix $\mathbf{C}$:

$$\mathbf{C} = \mathbf{H}^{-1}(\mathbf{B}\mathbf{T}) \tag{63}$$

Thus, the vector $\boldsymbol{\alpha}$ can be rewritten as:

$$\boldsymbol{\alpha} = \mathbf{C}\overline{\mathbf{W}} \tag{64}$$

Substituting Eq. (64) in to (62), we can obtain the expression of w_α in terms of $\overline{\mathbf{W}}$:

$$w_\alpha = \mathbf{R}^{\mathrm{T}}\mathbf{C}\overline{\mathbf{W}} \tag{65}$$

Next, we move on to express w_A in terms of $\overline{\mathbf{W}}$. From Eqs. (58), (61) and (65), we have:

$$w_A = \mathbf{S}^{\mathrm{T}}\, \mathbf{A} = w - \mathbf{R}^{\mathrm{T}}\mathbf{C}\overline{\mathbf{W}} \tag{66}$$

Evaluating w_A at the three nodes, we can obtain:

$$w_A(x_i, y_i) = \mathbf{S}^{\mathrm{T}}(x_i, y_i)\, \mathbf{A} = \overline{w}_i - \mathbf{R}^{\mathrm{T}}(x_i, y_i)\, \mathbf{C}\overline{\mathbf{W}}, \quad i = 1, 2, 3 \tag{67}$$

which give us the following matrix equation:

$$\underbrace{\begin{bmatrix} 1 & x_1 & y_1 \\ 1 & x_2 & y_2 \\ 1 & x_3 & y_3 \end{bmatrix}}_{\mathbf{M}_A} \mathbf{A} = \begin{bmatrix} \overline{w}_1 \\ \overline{w}_2 \\ \overline{w}_3 \end{bmatrix} - \underbrace{\begin{bmatrix} x_1^2 & x_1 y_1 & y_1^2 & x_1^3 & x_1^2 y_1 & x_1 y_1^2 & y_1^3 \\ x_2^2 & x_2 y_2 & y_2^2 & x_2^3 & x_2^2 y_2 & x_2 y_2^2 & y_2^3 \\ x_3^2 & x_3 y_3 & y_3^2 & x_3^3 & x_3^2 3_2 & x_3 y_3^2 & y_3^3 \end{bmatrix}}_{\mathbf{M}_\alpha} \mathbf{C}\overline{\mathbf{W}} \tag{68}$$

Since

$$\begin{bmatrix} \overline{w}_1 \\ \overline{w}_2 \\ \overline{w}_3 \end{bmatrix} = \underbrace{\begin{bmatrix} 1 & 0 & 0 & 0 & 0 & 0 & 0 & 0 & 0 \\ 0 & 0 & 0 & 1 & 0 & 0 & 0 & 0 & 0 \\ 0 & 0 & 0 & 0 & 0 & 0 & 1 & 0 & 0 \end{bmatrix}}_{\mathbf{B}_A} \overline{\mathbf{W}} \tag{69}$$

we can obtain $\mathbf{A}$ as:

$$\mathbf{A} = \mathbf{M}_A^{-1}\left(\mathbf{B}_A - \mathbf{M}_\alpha\, \mathbf{C}\right)\overline{\mathbf{W}} \tag{70}$$

Using Eq. (61), we obtain:

$$w_A = \mathbf{S}^{\mathrm{T}}\mathbf{M}_A^{-1}\left(\mathbf{B}_A - \mathbf{M}_\alpha\,\mathbf{C}\right)\overline{\mathbf{W}} \tag{71}$$

Combining with Eq. (65), we obtain the expression of w:

$$w = \mathbf{S}^{\mathrm{T}}\mathbf{M}_A^{-1}\left(\mathbf{B}_A - \mathbf{M}_\alpha\,\mathbf{C}\right)\overline{\mathbf{W}} + \mathbf{R}^{\mathrm{T}}\mathbf{C}\overline{\mathbf{W}} = \mathbf{N}_w\,\overline{\mathbf{W}} \tag{72}$$

where the matrix $\mathbf{N}_w$ (1×9) can be extracted as:

$$\mathbf{N}_w = \mathbf{S}^{\mathrm{T}}\mathbf{M}_A^{-1}(\mathbf{B}_A - \mathbf{M}_\alpha\mathbf{C}) + \mathbf{R}^{\mathrm{T}}\mathbf{C} \tag{73}$$

2.4.3. Shape functions of θ

Using the cubic polynomial expression of w from Eq. (13), θ_x can be expressed as:

$$\theta_x = \frac{\partial w}{\partial x} = A_2 + 2\alpha_1 x + \alpha_2 y + 3\alpha_4 x^2 + 2\alpha_5 xy + \alpha_6 y^2 \tag{74}$$

Similarly as in the case of w, the expression of the above rotations can also be divided into two parts, one containing the A coefficients only and another the α coefficients only:

$$\theta_x = A_2 + \theta_{x\alpha} \tag{75}$$

Since A_2 is part of the vector $\mathbf{A}$ which has been expressed in Eq. (70), we have:

$$A_2 = \mathbf{B}_x\mathbf{A} = \mathbf{B}_x\mathbf{M}_A^{-1}(\mathbf{B}_A - \mathbf{M}_\alpha\mathbf{C})\overline{\mathbf{W}} \tag{76}$$

where $\mathbf{B}_x$ is a Boolean matrix:

$$\mathbf{B}_x = \begin{bmatrix} 0 & 1 & 0 \end{bmatrix} \tag{77}$$

The expression $\theta_{x\alpha}$ can be written as:

$$\theta_{x\alpha} = \mathbf{R}_x^{\mathrm{T}}\boldsymbol{\alpha} = \mathbf{R}_x^{\mathrm{T}}\mathbf{C}\overline{\mathbf{W}} \tag{78}$$

where Eq. (64) is used to express $\boldsymbol{\alpha}$ and $\mathbf{R}_x$ is also a vector of local coordinates:

$$\mathbf{R}_x = \begin{bmatrix} 2x & y & 0 & 3x^2 & 2xy & y^2 & 0 \end{bmatrix}^{\mathrm{T}} \tag{79}$$

Substituting the expressions above into Eq. (74), the expression of θ_x is

$$\theta_x = \mathbf{B}_x\mathbf{M}_A^{-1}(\mathbf{B}_A - \mathbf{M}_\alpha\mathbf{C})\overline{\mathbf{W}} + \mathbf{R}_x^{\mathrm{T}}\mathbf{C}\overline{\mathbf{W}} \tag{80}$$

The shape function $\mathbf{N}_x$ of rotation θ_x is therefore:

$$\mathbf{N}_x = \mathbf{B}_x\mathbf{M}_A^{-1}(\mathbf{B}_A - \mathbf{M}_\alpha\mathbf{C}) + \mathbf{R}_x^{\mathrm{T}}\mathbf{C} \tag{81}$$

The derivation of shape function $\mathbf{N}_y$ for rotation θ_y is very similar to that for θ_x and is omitted here for brevity.

2.4.4. $\mathbf{B}_{\mathrm{CE}}$ matrix

Once we have determined the shape functions, the next step is to assemble the $\mathbf{B}_{\mathrm{CE}}$ matrix that relates the DoFs vector $\mathbf{q}_{\mathrm{CE}}$ to the opening vector $\boldsymbol{\Delta}$ (c.f. Eq. (56)). Substituting the shape functions in Eqs. (73) and (81) to express the w and θ terms in Eqs. (50), (54), and (55), the expression of $\mathbf{B}_{\mathrm{CE}}$ can be obtained as the following:

$$\mathbf{B}_{\mathrm{CE}} = \begin{bmatrix} 0 & 0 & 0 & 0 & 0 & 0 & -\mathbf{N}_w & 0 & 0 & 0 & 0 & 0 & 0 & \mathbf{N}_w \\ -L_1 & 0 & -L_2 & 0 & -L_3 & 0 & \frac{h^{\mathrm{bot}}}{2}\mathbf{N}_x & L_1 & 0 & L_2 & 0 & L_3 & 0 & \frac{h^{\mathrm{top}}}{2}\mathbf{N}_x \\ 0 & -L_1 & 0 & -L_2 & 0 & -L_3 & \frac{h^{\mathrm{bot}}}{2}\mathbf{N}_y & 0 & L_1 & 0 & L_2 & 0 & L_3 & \frac{h^{\mathrm{top}}}{2}\mathbf{N}_y \end{bmatrix} \tag{82}$$

2.4.5. $\mathbf{D}_{\mathrm{CE}}$ matrix

The relationship between traction $\boldsymbol{\tau}$ and opening vector $\boldsymbol{\Delta}$ is expressed through the constitutive matrix $\mathbf{D}_{\mathrm{CE}}$:

$$\boldsymbol{\tau} = \mathbf{D}_{\mathrm{CE}}\,\boldsymbol{\Delta}, \quad \mathbf{D}_{\mathrm{CE}} = \begin{bmatrix} (1-d_{\mathrm{I}})K & 0 & 0 \\ 0 & (1-d)K & 0 \\ 0 & 0 & (1-d)K \end{bmatrix} \tag{83}$$

where K and d are the penalty stiffness and the damage variable of the CE, respectively. The damage variable d in this work is updated by the bi-linear cohesive law proposed by Turon et al. [42,43]. The damage variable d_{I} under Mode I loading is distinguished from d to avoid interpenetration of the top and bottom surfaces under compression:

$$d_{\mathrm{I}} = \begin{cases} d, & \Delta_{\mathrm{I}} \geq 0 \\ 0, & \Delta_{\mathrm{I}} < 0 \end{cases} \tag{84}$$

The penalty stiffness K is set as:

$$K = \alpha \frac{E_3}{t} \tag{85}$$

where E_3 is the out-of-plane laminate Young's modulus, t is the thickness of the laminate and α is a constant: not to be confused with the matrix $\boldsymbol{\alpha}$ used in Eq. (64), here set to be 50 [8].

2.4.6. Stiffness matrix and residual vector

In this work, the secant stiffness matrix is used as the stiffness matrix of the CE:

$$\mathbf{K}_{\mathrm{CE}} = \int_{\Gamma} \mathbf{B}_{\mathrm{CE}}^{\mathrm{T}}\, \mathbf{D}_{\mathrm{CE}}\, \mathbf{B}_{\mathrm{CE}}\, \mathrm{d}\,\Gamma \tag{86}$$

where Γ represents the domain of the interface. The integral in Eq. (86) is hard to calculate analytically. Thus, the Gaussian integration scheme is applied to obtain the stiffness matrix numerically. Earlier works have shown that using a higher number of quadrature points improves the accuracy and smoothness of the load–displacement solutions of delamination simulations [23,33,36]. Therefore, thirteen quadrature points are used in this work for the integration of the structural CE, with their coordinates and weights taken from the work of Cowper [44].

Assuming that no external distributed loads are applied to the cohesive interfaces, only the internal force vector of the CE contributes to the overall residual vector of the system. The residual vector contribution from this CE can then be written as:

$$\mathbf{f}_{\mathrm{res}} = -\mathbf{f}_{\mathrm{int}} = -\mathbf{K}_{\mathrm{CE}}\, \mathbf{q}_{\mathrm{CE}} \tag{87}$$

Note that although the cohesive element developed in this paper appears to have finite thickness between its nodes, the actual integration domain is in fact the zero-thickness interface between the plies. The finite thickness of the cohesive element is entirely due to the fact that the nodes of the cohesive element, shared with the top and bottom ply elements, are positioned on the midplanes of the plies. Through kinematic derivations, the displacements at the upper and lower surfaces of the interface are obtained. The separation vector is then calculated as the differences between them. Subsequently, the corresponding tractions and damage variables are calculated using the penalty stiffness and the cohesive law. Thus, the cohesive behaviour at the zero-thickness interface can be achieved even though the cohesive element has finite thickness between its nodes. In the situation where the physical thickness of the interface, i.e., the resin-rich region between two plies, is a matter of importance, different considerations may apply. If the membrane stiffness of the resin-rich region cannot be neglected, then solid elements would be needed to model this region. In general, however, the membrane stiffness of the resin-rich region is negligible, hence a cohesive law can still be assumed to represent the out-of-plane behaviour of the interface. We have developed an approach which relates the finite thickness of the resin-rich region to material properties and the penalty stiffness of the traction–separation law. This is the subject of a future communication.

3. Results

The structural elements Section 2 have been implemented in the Abaqus user-defined element subroutines. The structural CE model was firstly verified on the three classical benchmarks, namely the double cantilever beam (DCB), the end-notched flexure (ENF), and the mixed-mode bending (MMB) problems. As the above benchmarks only pertain to unidirectional laminates, a multi-directional laminate problem, namely the single-leg bending (SLB) problem [45,46], was simulated to demonstrate the 3D capacity of the model. All simulations of the structural CE model were performed in implicit analysis using the Quasi-Newton solver without damping or viscosity. The reference solutions on these problems were obtained with analytical equations and Abaqus standard FE simulations using 8-node linear solid elements (C3D8I element in Abaqus) for the plies and 8-node linear CEs for the interfaces. The linear CEs were implemented as user-defined elements following the formulation in [5], with the cohesive law from Turon et al. [42,43]. The problem descriptions and modelling details will be presented in this section, followed by comparisons of load–displacement curves and computational time.

3.1. Unidirectional laminate benchmarks: DCB, ENF, and MMB

3.1.1. Description of the unidirectional laminate tests

The unidirectional laminate benchmarks are drawn from the work by Krueger [46], except that the pre-crack length of the ENF model is increased to 35 mm in this work to avoid the snapback in load–displacement response. The geometric parameters and boundary conditions are shown in Fig. 6 and Table 1. The detailed material properties are shown in Tables 2 and 3. The mixed mode ratio of the SLB specimen is approximately 40% mode II (G_{II} / G_{T}=0.4) and the MMB specimen is 0.5 (G_{II} / G_{T}=0.5).

3.1.2. Description of the model

Since the plies of the benchmarks in this section are all 0°, the symmetric lay-up conditions in Eq. (2) are met. Therefore, the structural model could simply use one layer of shell elements on each side of the delamination, with one layer of structural CEs in between. The Abaqus solid models are built according to the work of Krueger [46], except that CEs, instead of VCCT, are used to model delamination.

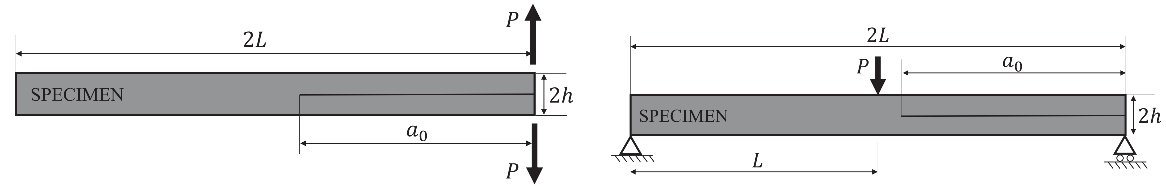

(a) DCB (b) ENF

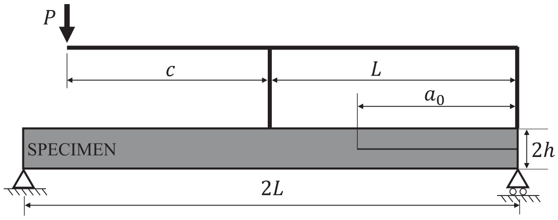

(c) MMB

Fig. 6. DCB, ENF, and MMB test specimens.

Table 1
Geometric parameters for unidirectional benchmarks.

Model \ Param. (mm)	$2L$	a_0	h	b (width)	c
DCB	150.0	30.5	1.50	25.0	–
ENF	101.6	35.0	2.25	25.4	–
MMB	100.8	25.4	2.25	25.4	41.3

Table 2
Material properties for DCB [46].

T300/1076 Unidirectional graphite/epoxy prepreg		
E_{11}= 139.4 GPa	E_{22}= 10.16 GPa	E_{33} = 10.16 GPa
ν_{12} = 0.30	ν_{13} = 0.30	ν_{23} = 0.436
G_{12} = 4.6 GPa	G_{13} = 4.6 GPa	G_{23} = 3.54 GPa
Fracture toughness data		
$G_{\mathrm{Ic}} = 0.170$ kJ/m^2	$G_{\mathrm{IIc}} = 0.494$ kJ/m^2	$\eta = 1.62$
Interfacial strength data [20,43]		
$\tau_{\mathrm{Ic}} = 30$ MPa	$\tau_{\mathrm{IIc}} = 60$ MPa	

Table 3
Material properties for ENF and MMB [46].

IM7/8552 Unidirectional graphite/epoxy prepreg		
E_{11}= 161 GPa	E_{22}= 11.38 GPa	E_{33} = 11.38 GPa
ν_{12} = 0.32	ν_{13} = 0.32	ν_{23} = 0.45
G_{12} = 5.2 GPa	G_{13} = 5.2 GPa	G_{23} = 3.9 GPa
Fracture toughness data		
$G_{\mathrm{Ic}} = 0.212$ kJ/m^2	$G_{\mathrm{IIc}} = 0.774$ kJ/m^2	$\eta = 2.1$
Interfacial strength data [20,43]		
$\tau_{\mathrm{Ic}} = 30$ MPa	$\tau_{\mathrm{IIc}} = 60$ MPa	

3.1.3. Load–displacement curves

The load–displacement curves obtained from the simulations are shown in Fig. 7. The designations “-solid” and “-structural” denote the results of the traditional solid element model and those of the proposed structural CE model, respectively. The results on meshes of different element sizes are plotted together with the analytical solutions [47–49].

The DCB results in Fig. 7 indicated that the standard model with solid elements requires that the element size should not exceed 0.5 mm. When the element sizes are greater than or equal to 1 mm, the simulation results differ greatly from the analytical solution. The error on peak load exceeds 30%, and the post-peak curve also stays way above the analytical one. With the proposed structural model, the results on 2-mm mesh remain in close agreement with the analytical solution, with a less than 3% error on the peak load. The post-peak curve also closely follows the analytical curve. The slight over-prediction of the stiffness is expected as a result of neglecting transverse shear in the Kirchhoff–Love shell elements. The analytical solution based on the corrected beam theory, however, includes such transverse shear effect [47]. Even on a 5-mm mesh, the structural model can predict the peak load fairly

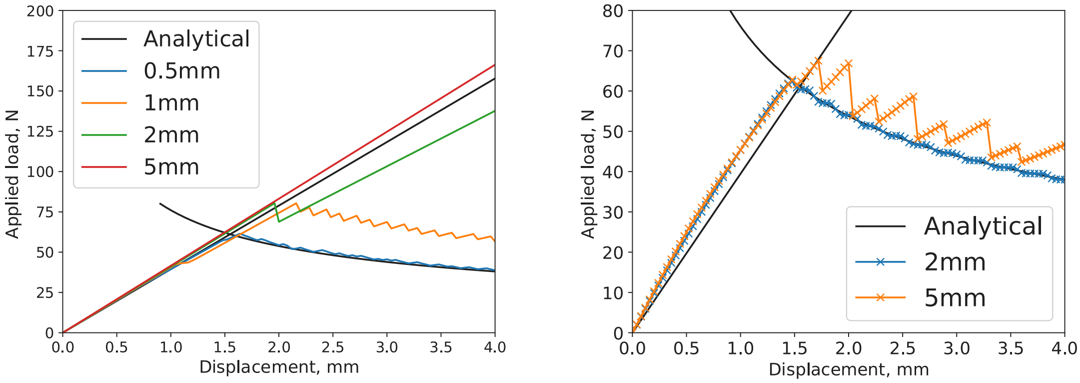

(a) DCB-Solid (b) DCB-Structural

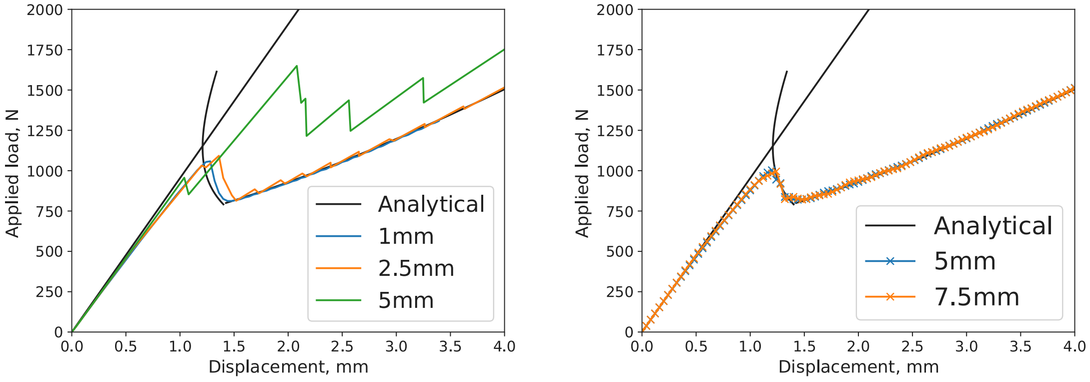

(c) ENF-Solid (d) ENF-Structural

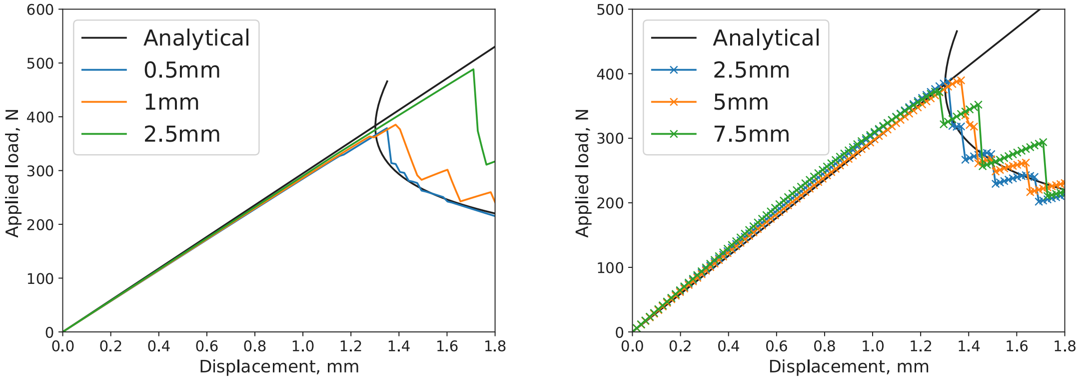

(e) MMB-Solid (f) MMB-Structural

Fig. 7. Results of the DCB, ENF, and MMB tests, showing the sensitivities of the conventional solid CE and the proposed structural CE on different mesh densities.

well despite the post-peak oscillations right above the analytical curve. Such oscillations are due to the larger spacing between the integration points on coarser meshes.

In the ENF case, the solid element model on 1-mm mesh could capture the peak load correctly, thanks to the larger cohesive zone in Mode II delamination than in Mode I. However, the result on 2.5-mm mesh already shows a clear drift towards over-prediction. As the element size increases to 5 mm, the peak load and post-peak response again become severely over-predicted. Correspondingly, if the structural model is used on the 5-mm mesh, the predicted curve remains close to the analytical solution throughout the loading history. Even the 7.5-mm structural model manages to capture the load–displacement response very accurately. The slight

Table 4
Comparison of CPU time (unit: second).

	DCB	ENF	MMB
Solid model (mesh size)	5311.8 (0.5 mm)	4239.7 (1 mm)	5560.7 (0.5 mm)
Structural model (mesh size)	197.15 (5 mm) 836.76 (2 mm)	285.33 (7.5 mm) 736.41 (5 mm)	370.02 (7.5 mm) 474.79 (5 mm)
Reduction by structural	96.3% 84.2%	93.3% 82.6%	93.3% 91.5%

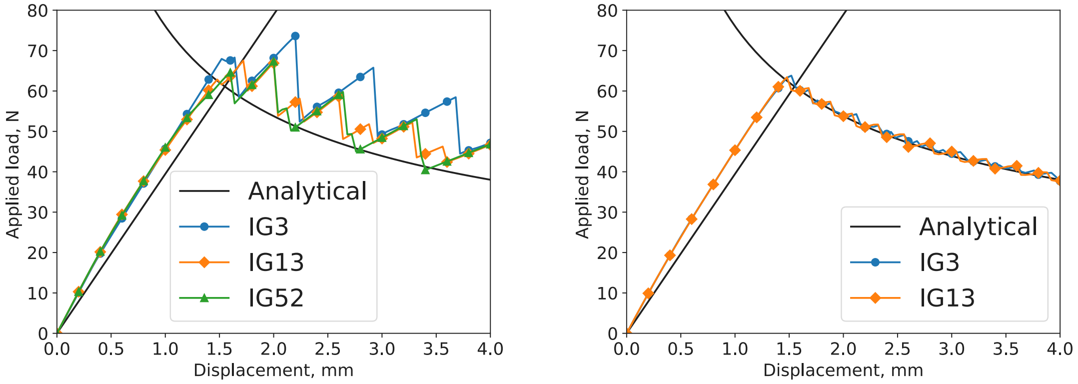

(a) Results on 5-mm mesh (b) Results on 2-mm mesh

Fig. 8. Load–displacement curves of the DCB model with different integration points on two different meshes.

under-prediction of the peak load is expected, as the analytical curve is based on Linear Elastic Fracture Mechanics, which ignores the presence of material softening (i.e. the cohesive zone) at the crack tip.

In the MMB case, very similar trends can be observed. The solid model on the 2.5-mm mesh cannot capture the correct load–displacement response, while the structural model's predictions on the 2.5-mm and 5-mm meshes oscillate closely around the analytical curve. Even the 7.5-mm structural model predicts the peak load correctly, albeit with bigger oscillations during the load drop section due to the coarser distribution of integration points in larger elements.

3.1.4. Computational performances

By allowing larger elements to be used, the proposed structural model is able to reduce the computational time of the delamination simulations considerably. The results of the structural model are compared against those of the solid element model. The comparison of CPU time is reported in Table 4. It can be seen that the structural model can reduce the computational time in all three problems by more than 90%, while retaining accurate predictions of the peak loads and the overall load-drop curves.

3.1.5. Studies on integration points

In this section, the influence of the number of integration points in one element on the simulation results is discussed, using the error of the load–displacement curves with respect to the analytical solutions. The earlier work in 2D [23] showed the largest influence of integration points in the DCB model. Therefore, only DCB is studied here. The load–displacement curves with different integration points are reported in Fig. 8. The use of 52 integration points in the element domain is achieved through subdomain integration as detailed in Tosti Balducci and Chen [36].

From Fig. 8(a), on the 5-mm mesh, it is clear that as we increase the number of integration points, the predicted curves become closer to the analytical one, consistent with earlier results [23,36]. It is also clear that even with just 3 integration points, the prediction does not exhibit the same overshoot of peak load as seen in the solid-element model in Fig. 7(a). This indicates that it is the higher-order continuity in the kinematics of the structural elements that brings down this overshoot and hence enables the use of larger elements. From Fig. 8(b), on the 2-mm mesh, the number of integration points does not seem to show any effect. In summary, having more integration points increases the prediction accuracy on coarse meshes, but has little effect once the mesh is sufficiently refined. This suggests a trade-off between using more integration points and using finer meshes. As the element size determines the size of the system matrix, while the operations at integration points are local to each element and can be parallelized, it would be more efficient to use more integration points on a coarser mesh.

3.2. Unidirectional laminate benchmarks: Reinforced DCB

Although the earlier benchmarks are modelled in 3D, they can actually be modelled in 2D [23] as the delamination front does not vary significantly across the width of the specimens. To verify the capacity of the proposed elements in modelling delamination in 3D, the Reinforced DCB (R-DCB) problem is studied in this section.

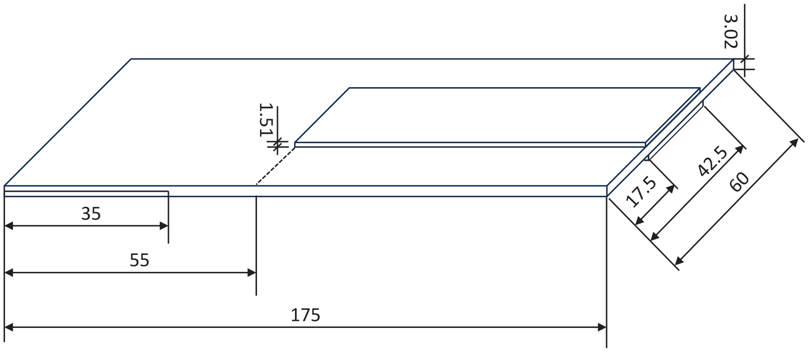

Fig. 9. Geometry of the R-DCB specimen (units in mm) [50].

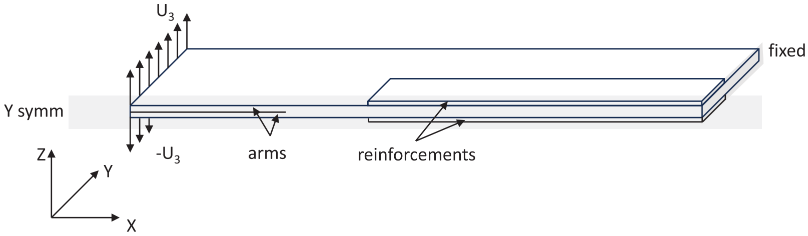

Fig. 10. Boundary conditions and loading of the finite element model; U$_3$=7.5 mm.

Table 5
Lamina properties of the R-DCB model [51].

Property	Value	Units
E_{11}	154	GPa
$E_{22} = E_{33}$	8.5	GPa
$G_{12} = G_{13}$	4.2	GPa
G_{23}	3.04	GPa
$\mu_{12} = \mu_{13}$	0.35	–
μ_{23}	0.4	–

Table 6
Interlaminar properties of the R-DCB model [51].

Property	Value	Units
K: Penalty stiffness	10^5	N/mm^3
G_{Ic}	0.305	N/mm
G_{IIc}	2.77	N/mm
η	2.05	–
τ_{Ic}	32.6	MPa
τ_{IIc}	98	MPa

3.2.1. Description of the reinforced DCB

The R-DCB experiment was proposed by Carreras et al. [50]. The main part of the R-DCB specimen is a standard DCB specimen made of 16 unidirectional plies at 0°. Two reinforcement parts, made of 8 plies of the same material at 0°, are attached on the top and bottom of the DCB specimen. The elastic properties of the ply material are shown in Table 5. The pre-crack is 35 mm long on the opposite side of the reinforcement. The geometry of the R-DCB specimen is shown in Fig. 9.

The R-DCB problem is modelled with the proposed structural elements. Symmetry is used to reduce the size of the model. The boundary conditions of the model are shown in Fig. 10. The right side of the model is fixed and a displacement loading is applied on the left side. The two arms of the DCB and the two reinforcement parts are each modelled with one layer of cubic shell elements. Their interfaces are each modelled with one layer of structural CEs. The properties for the structural CEs are shown in Table 6.

3.2.2. Results and comparisons

Similarly as in the previous section, different mesh sizes are used for mesh convergence analysis. The predicted load–displacement curves on different mesh sizes are shown in Fig. 11. We can see that the three curves agree well with each other. The 5-mm curve

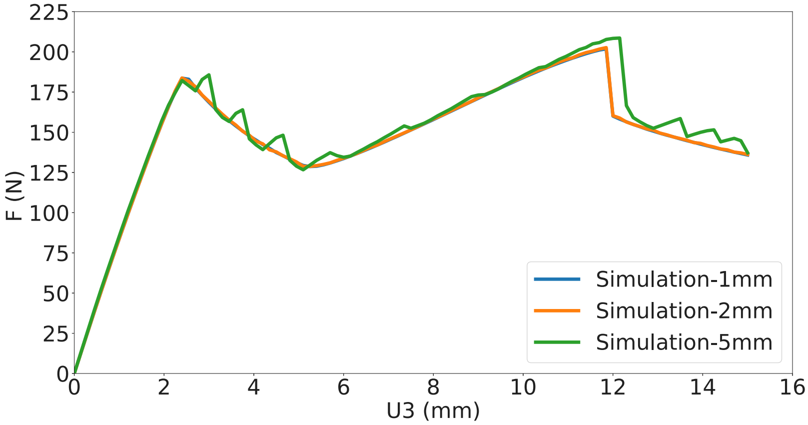

Fig. 11. Load–displacement curves of the reinforced DCB with different mesh sizes from simulation results.

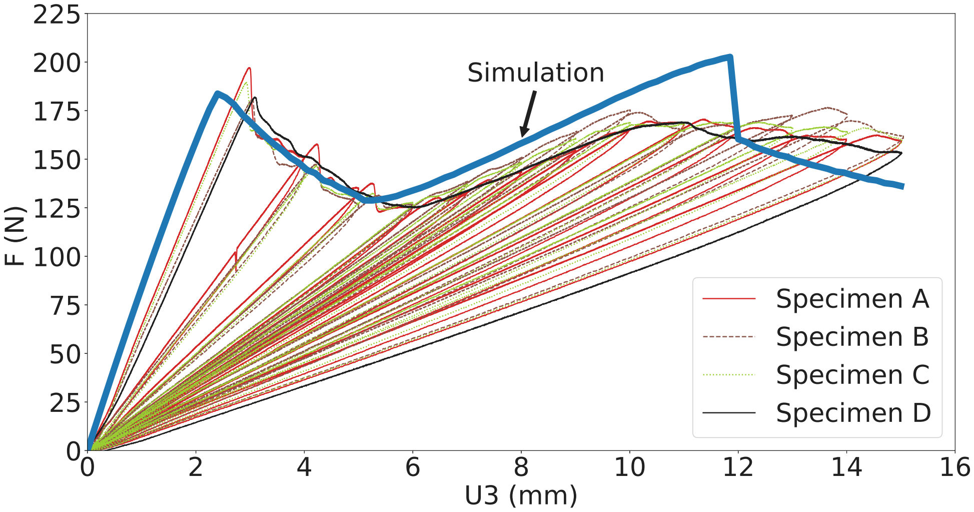

Fig. 12. Comparison of numerical and experimental results of the force–displacement curves [50].

is not as smooth as the other two, consistent with the DCB results in Fig. 7(b). The most obvious difference is that the 5-mm curve slightly over-predicts the second peak load and the corresponding opening displacement. The 2-mm and 1-mm curves fall on top of each other, indicating that the mesh has converged. The 2-mm curve is used for subsequent comparison with experimental data.

In Fig. 12, it can be seen that the predicted load–displacement curve agrees reasonably well with the experimental data from 4 specimens. However, there are three obvious differences. Firstly, the initial stiffness is greater than the experimental one. This could be due to the fact that the loading grips and test machine increase compliance, which is not included in the model. Looking closely at the initial part of the experimental load–displacement curves, we can see that there is a slight increase in stiffness at around 0.5 mm displacement. This indicates the presence of some initial machine compliance, which is not taken into account in the simulation. Secondly, for the second peak load that denotes the onset of delamination in the reinforced region, the numerical prediction is greater than the experimental result by 15%. This could be due to the lack of transverse shear compliance in the model, particularly in the reinforced region. This leads to a stiffer response in the model than in the experiments when the reinforced region is loaded. This stiffer reinforcement slows down the delamination propagation when it first encounters the reinforcement, leading to slower damage creation. Third, the numerical curve after the second peak falls sharply and below the experimental curves. This indicates that the fracture toughness value used by the structural CEs may have underestimated the fracture energy for the crack propagation in the reinforced region, which may include crack toughening mechanisms such as fibre bridging due to the curved delamination front.

In Fig. 13, the positions of the crack fronts of the test specimens and numerical models are plotted at multiple opening displacements. It can be observed that the delamination front shapes of the numerical results are consistent with the experimental results: the delamination front is a straight line before it goes into the reinforced part. When it extends to the reinforced region, the shape changes from a straight line to a curve. However, the delamination propagates faster in the numerical results than in

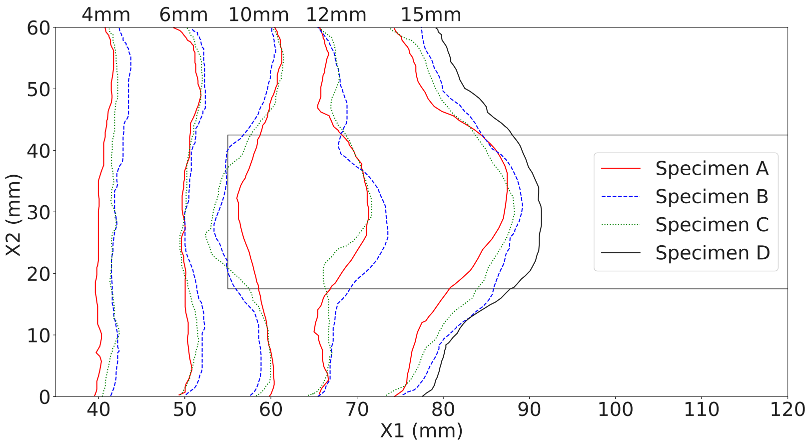

(a) Experiment results [50]

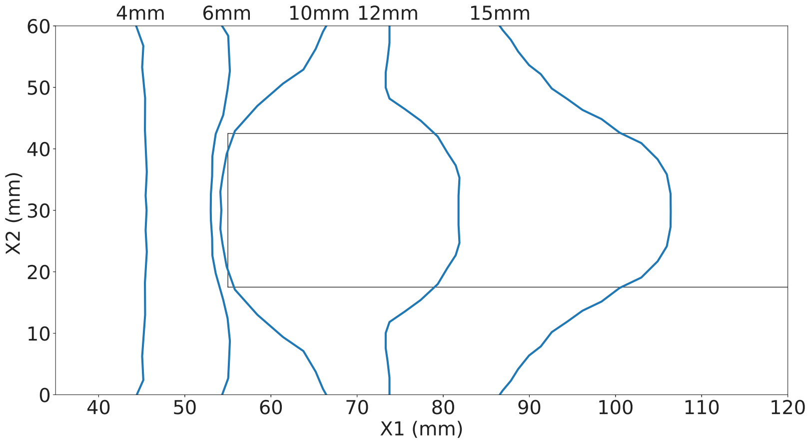

(b) Numerical results

Fig. 13. Comparison of numerical and experimental results of the delamination front position.

the experiments, except at 10-mm displacement when the delamination propagation in the middle is clearly hindered by the stiff reinforcement. However, once delamination initiates in the reinforced region, it again propagates faster in the simulation than in the experiment, as shown by the curves at 12-mm and 15-mm displacements. The reason for the faster numerical propagation could be that the stiffness in the simulation is higher than that in the experiments due to the lack of initial machine compliance and the lack of transverse shear compliance in the model. Therefore, in the simulation, a smaller displacement loading on the arms would be needed than in the experiments to open the cohesive crack tip to reach its delamination onset. This also means that for the same amount of displacement loading, the simulation would predict the delamination front to propagate further than in the experiments.

3.3. Multi-directional laminate benchmark: SLB

3.3.1. Description of the SLB test

The SLB specimen is shown in Fig. 14, with its geometrical parameters specified in Table 7. Unlike in the previous benchmarks, the ply angles here are no longer all 0°. The material of the SLB model is C12K/R6376 and its properties are shown in Table 8. Unfortunately, The value of τ_{IIc} cannot be found in the literature. However, the value of τ_{IIc} can be estimated by τ_{Ic} in Eq. (88) which is derived by the equations in Ref. [43] with the same penalty stiffness of mode I and mode II. Hence, the value of τ_{IIc} here is estimated to be 58 MPa.

$$\tau_{\text{IIc}} = \tau_{\text{Ic}} \sqrt{\frac{G_{\text{IIc}}}{G_{\text{Ic}}}} \tag{88}$$

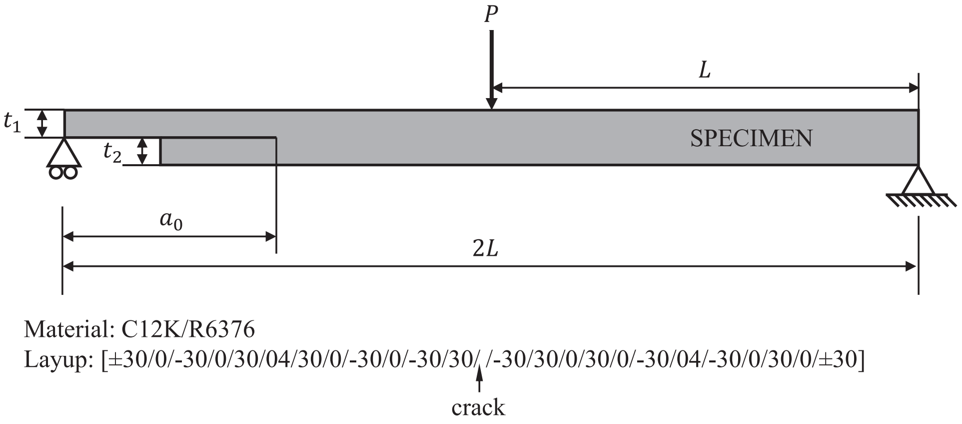

Fig. 14. SLB specimen [45].

Table 7
Geometric parameters for the SLB specimen.

Parameter	$2L$	a_0	t_1	t_2	b (width)
value (mm)	177.8	60	2	2	25.4

Table 8
C12K/R6376 material properties for SLB specimen [46].

E_{11}= 146.9 GPa	E_{22}= 10.6 GPa	E_{33} = 10.6 GPa
ν_{12} = 0.33	ν_{13} = 0.33	ν_{23} = 0.33
G_{12} = 5.45 GPa	G_{13} = 5.45 GPa	G_{23} = 3.99 GPa
Fracture toughness data		
G_{Ic} = 0.34 kJ/m^2	G_{IIc} = 1.286 kJ/m^2	η = 3.39
Interfacial strength data		
τ_{Ic} = 25 MPa [52]	τ_{IIc} = 58 MPa[a]	

[a] Estimated [20].

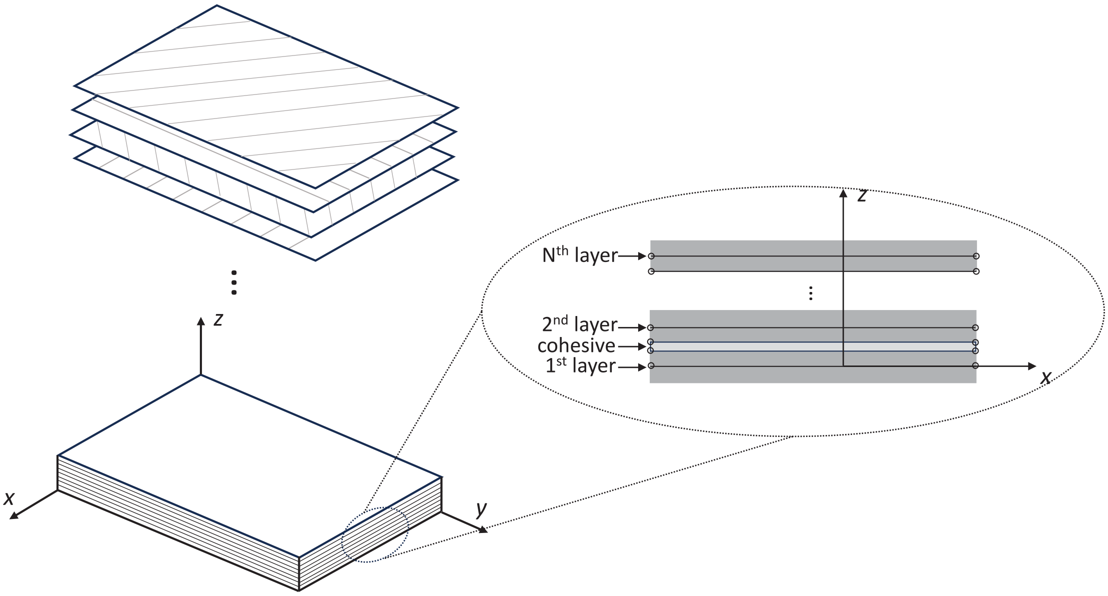

Fig. 15. Layer-wise model for SLB.

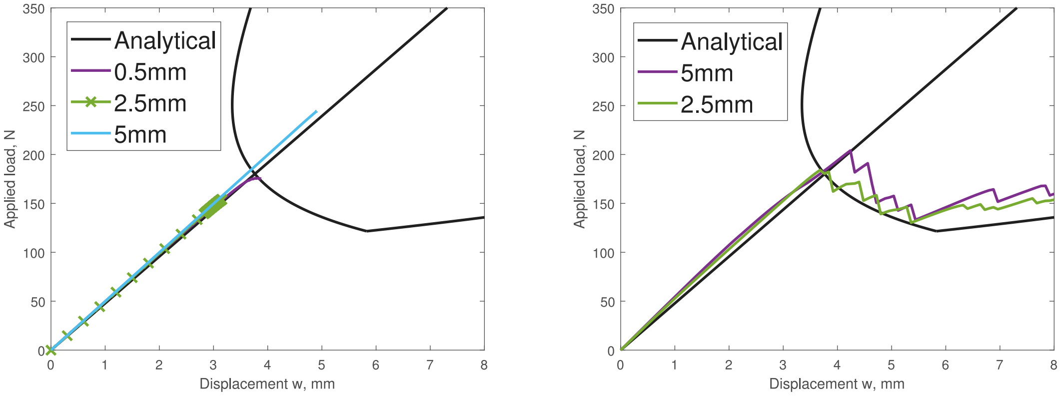

(a) SLB-Solid (b) SLB-Structural

Fig. 16. Load–displacement predictions of the SLB.

3.3.2. Description of the model

Since the SLB specimen is a multi-directional laminate and its lay-up is not symmetric, we can no longer model the entire laminate with a single layer of shell elements on each side of the delamination, as done in the unidirectional models. Therefore, the SLB model uses one layer of shell elements for each ply and one layer of structural CEs between every two plies (c.f., Fig. 15).

3.3.3. Load–displacement curves

In Fig. 16, the load–displacement curves are reported for the solid and structural models. Both are compared with the analytical solution derived in Appendix C. All the load–displacement predictions by the solid model could not reach numerical convergence within the allowable settings on solver iterations. As a result, the load-decreasing section of the curve could not be obtained. From the left figure, it can be seen that only the 0.5-mm solid model can capture the correct peak load. For the 2.5-mm solid model, the peak load is much lower than the analytical solution due to premature divergence of analysis. However, the peak load of the model on the 5-mm mesh is much larger than the analytical solution, in line with the solid model's performance in the unidirectional benchmarks. The right figure shows that all the structural models can obtain converged solutions throughout the full loading history. Overall speaking, the predicted curves of the structural models follow well the analytical solution. On the 2.5-mm mesh, the error of peak load is 2%, the same level of accuracy as that of the unidirectional structural model. On the 5-mm mesh, the predicted peak load is larger by 12.5%. However, the post-peak part of the curve quickly converges to that of the 2.5-mm mesh result. It should be noted that the initial stiffness of the structural models is 5% larger than that of the analytical solution. The reason is that the compliance C obtained by Eq. (C.12) is calculated by simplifying the SLB model into a 2D beam model (c.f., Fig. C.1), where the neutral axis is assumed to be aligned with the centreline of the uncracked region for simplicity. However, the actual neutral axis of the SLB model should be slightly above the assumed one, as only the top part of the cracked region would be under bending. This discrepancy would cause the analytical stiffness to be slightly lower than that in the actual situation. Another discrepancy to note is that when the crack length a is longer than L, the load increases again with increasing displacement (c.f., Appendix C, curve DFE). For this part, the predicted curves of the structural models are above the analytical curve. This discrepancy is however expected. As the crack length a increases with delamination propagation, the mixed-mode ratio B is found to also increase, particularly when $a > L$ [53], which causes the critical energy release rate G_c to increase as well. However, the analytical solution in Appendix C assumes a fixed mixed-ratio, which underestimates G_c for $a > L$, hence resulting in the analytical curve being below the numerical ones. The analytical curve could be corrected, should an analytical expression of G_c in terms of a become available.

In addition, it needs to be emphasized that the difficulty of convergence of the solid model leads to a significant increase in computational time. Due to this reason, artificial viscosity would be needed to continue the simulation through the convergence difficulties. However, this would introduce a fitting parameter which generally requires trial and error to properly set its value. This suggests that the proposed structural model not only allows coarser meshes with faster computations but also ensures better numerical stability than the solid element model.

4. Summary and conclusions

This work aims to establish a state-of-the-art numerical method to simulate the delamination of composite laminates aimed at overcoming the cohesive zone limit on mesh density. The Kirchhoff–Love triangular cubic plate element from Allman [40] has been extended for the modelling of symmetric laminate shells. A structural CE, conforming with the shell element, has been developed to model delamination between the shells. The combination of the Kirchhoff–Love shell element and the structural CE is shown to be a powerful new method that overcomes the cohesive zone limit and models delamination with high accuracy and efficiency under different loading conditions. This capability is expected to make a strong impact in the composites modelling community, as the cohesive zone limit has been a long-lasting and well-known problem for delamination modelling.

This method has also been validated on the DCB, ENF, MMB, and SLB problems. The results show excellent agreement with the analytical solutions. By comparing the results with those from the solid element model, the structural model has shown the following advantages: (1) it can accurately predict the load–displacement curves with significantly coarser meshes than the solid element model, allowing 5-mm elements to be used instead of the 0.5-mm elements in the latter; (2) its computational speed is much faster than that of the solid element model, achieving more than 90% reduction in CPU time; and (3) it has better numerical stability than the solid element model, reaching convergence without needing artificial viscosity for stabilization. In addition, the method has been applied on the R-DCB problem where the delamination front is highly curved. Its predictions on the load–displacement curve and delamination fronts are in very good agreement with the experimental data.

Future work includes the incorporation of intralaminar damage in the structural model. Since Kirchhoff–Love thin shell elements are used to model the plies, the transverse strains are ignored. This will impact the prediction of intralaminar damage in the model because an accurate three-dimensional damage criterion would require out-of-plane stresses and/or strains as inputs. However, since the layer-by-layer modelling method used in this work employs CEs between every two plies, the required out-of-plane stresses can be obtained by extracting the tractions of the CEs and interpolating them between the layers [23]. This is the subject of an ongoing work in the group.

CRediT authorship contribution statement

Xiaopeng Ai: Writing – original draft, Visualization, Validation, Software, Methodology, Investigation, Funding acquisition, Formal analysis, Data curation. **Boyang Chen:** Writing – review & editing, Supervision, Resources, Project administration, Methodology, Funding acquisition, Conceptualization. **Christos Kassapoglou:** Writing – review & editing, Supervision, Resources, Project administration, Methodology, Funding acquisition.

Declaration of competing interest

The authors declare the following financial interests/personal relationships which may be considered as potential competing interests: Xiaopeng Ai reports financial support was provided by China Scholarship Council. If there are other authors, they declare that they have no known competing financial interests or personal relationships that could have appeared to influence the work reported in this paper.

Acknowledgements

The authors would like to acknowledge the useful discussions with Giorgio Tosti Balducci, PhD candidate in the same group. The first author would like to acknowledge funding support from the China Scholarship Council (No. 201906290034) for this research.

Appendix A. H matrix

Before we calculate U_0 in Eq. (3), we need to calculate six parts. The first part is:

$$\frac{D_{11}}{2}\left(\frac{\partial^2 w}{\partial x^2}\right)^2 = D_{11}(2\alpha_1^2 + 12x\alpha_1\alpha_4 + 4y\alpha_1\alpha_5 + 18x^2\alpha_4^2 + 12xy\alpha_4\alpha_5 + 2y^2\alpha_5^2) \tag{A.1}$$

Based on Eq. (16), we can obtain:

$$\iint_A \frac{D_{11}}{2}\left(\frac{\partial^2 w}{\partial x^2}\right)^2 \mathrm{d}x\mathrm{d}y = \frac{1}{2}\boldsymbol{\alpha}^{\mathrm{T}}\,\mathbf{H}_1\,\boldsymbol{\alpha} \tag{A.2}$$

where $\mathbf{H}_1$ is:

$$\mathbf{H}_1 = \iint_A D_{11}\begin{bmatrix} 4 & 0 & 0 & 12x & 4y & 0 & 0 \\ & 0 & 0 & 0 & 0 & 0 & 0 \\ & & 0 & 0 & 0 & 0 & 0 \\ & & & 36x^2 & 12xy & 0 & 0 \\ & \text{Symmetric} & & & 4y^2 & 0 & 0 \\ & & & & & 0 & 0 \\ & & & & & & 0 \end{bmatrix}\mathrm{d}x\mathrm{d}y \tag{A.3}$$

The second part is:

$$\frac{D_{22}}{2}\left(\frac{\partial^2 w}{\partial y^2}\right)^2 = D_{22}(2\alpha_3^2 + 4x\alpha_3\alpha_6 + 12y\alpha_3\alpha_7 + 2x^2\alpha_6^2 + 12xy\alpha_6\alpha_7 + 18y^2\alpha_7^2) \tag{A.4}$$

Then, an equation which is similar as Eq. (A.2) in terms of $\mathbf{H}_2$ can be obtained:

$$\iint_A \frac{D_{22}}{2}\left(\frac{\partial^2 w}{\partial x^2}\right)^2 \mathrm{d}x\mathrm{d}y = \frac{1}{2}\boldsymbol{\alpha}^{\mathrm{T}}\,\mathbf{H}_2\,\boldsymbol{\alpha} \tag{A.5}$$

where $\mathbf{H}_2$ is:

$$\mathbf{H}_2 = \iint_A D_{22} \begin{bmatrix} 0 & 0 & 0 & 0 & 0 & 0 & 0 \\ & 0 & 0 & 0 & 0 & 0 & 0 \\ & & 4 & 0 & 0 & 4x & 12y \\ & & & 0 & 0 & 0 & 0 \\ & \text{Symmetric} & & & 0 & 0 & 0 \\ & & & & & 4x^2 & 12xy \\ & & & & & 0 & 36y^2 \end{bmatrix} \mathrm{d}x\mathrm{d}y \tag{A.6}$$

The third part is:

$$D_{12}\frac{\partial^2 w}{\partial x^2}\frac{\partial^2 w}{\partial y^2} = D_{12}(4\alpha_1\alpha_3 + 4x\alpha_1\alpha_6 + 12x\alpha_3\alpha_4 + 12y\alpha_1\alpha_7 + 4y\alpha_3\alpha_5 \\ + 12x^2\alpha_4\alpha_6 + 12y^2\alpha_5\alpha_7 + 36xy\alpha_4\alpha_7 + 4xy\alpha_5\alpha_6) \tag{A.7}$$

and $\mathbf{H}_3$ can be obtained by using the same method:

$$\mathbf{H}_3 = \iint_A D_{12} \begin{bmatrix} 0 & 0 & 4 & 0 & 0 & 4x & 12y \\ & 0 & 0 & 0 & 0 & 0 & 0 \\ & & 0 & 12x & 4y & 0 & 0 \\ & & & 0 & 0 & 12x^2 & 36xy \\ & \text{Symmetric} & & & 0 & 4xy & 12y^2 \\ & & & & & 0 & 0 \\ & & & & & & 0 \end{bmatrix} \mathrm{d}x\mathrm{d}y \tag{A.8}$$

Therefore, the **H** matrix of 4th, 5th and 6th part are expressed by the following expressions:

$$\mathbf{H}_4 = \iint_A D_{16} \begin{bmatrix} 0 & 4 & 0 & 0 & 8x & 8y & 0 \\ & 0 & 0 & 12x & 4y & 0 & 0 \\ & & 0 & 0 & 0 & 0 & 0 \\ & & & 0 & 24x^2 & 24xy & 0 \\ & \text{Symmetric} & & & 16xy & 8y^2 & 0 \\ & & & & & 0 & 0 \\ & & & & & & 0 \end{bmatrix} \mathrm{d}x\mathrm{d}y \tag{A.9}$$

$$\mathbf{H}_5 = \iint_A D_{26} \begin{bmatrix} 0 & 0 & 0 & 0 & 0 & 0 & 0 \\ & 0 & 4 & 0 & 0 & 4x & 12y \\ & & 0 & 0 & 8x & 8y & 0 \\ & & & 0 & 0 & 0 & 0 \\ & \text{Symmetric} & & & 0 & 8x^2 & 24xy \\ & & & & & 16xy & 24y^2 \\ & & & & & & 0 \end{bmatrix} \mathrm{d}x\mathrm{d}y \tag{A.10}$$

and

$$\mathbf{H}_6 = \iint_A D_{66} \begin{bmatrix} 0 & 0 & 0 & 0 & 0 & 0 & 0 \\ & 4 & 0 & 0 & 8x & 8y & 0 \\ & & 0 & 0 & 0 & 0 & 0 \\ & & & 0 & 0 & 0 & 0 \\ & \text{Symmetric} & & & 16x^2 & 16xy & 0 \\ & & & & & 16y^2 & 0 \\ & & & & & & 0 \end{bmatrix} \mathrm{d}x\mathrm{d}y \tag{A.11}$$

The **H** matrix can be written as the sum of $\mathbf{H}_i$ $(i = 1, 2, \dots, 6)$:

$$\mathbf{H} = \mathbf{H}_1 + \mathbf{H}_2 + \mathbf{H}_3 + \mathbf{H}_4 + \mathbf{H}_5 + \mathbf{H}_6 \tag{A.12}$$

where the integral for each item of the **H** matrix can be calculated by using the formulas given in Ref. [37].

Appendix B. B matrix

Plugging the expression of w (Eq. (13)) into Eq. (2), we can express the moment resultants as:

$$M_x = -2D_{11}\alpha_1 - 2D_{16}\alpha_2 - 2D_{12}\alpha_3 - 6xD_{11}\alpha_4 - (2yD_{11} + 4xD_{16})\alpha_5 \\ - (2xD_{12} + 4yD_{16})\alpha_6 - 6yD_{12}\alpha_7 \tag{B.1}$$

which in matrix form is:

$$M_x = \mathbf{B}_{M_x}^{\mathrm{T}}\,\boldsymbol{\alpha} \tag{B.2}$$

where $\mathbf{B}_{M_x}^{\mathrm{T}}$ is:

$$\begin{aligned}\mathbf{B}_{M_x}^{\mathrm{T}} = [&-2D_{11}, -2D_{16}, -2D_{12}, -6xD_{11}, -(2yD_{11}+4xD_{16}),\\ &-(2xD_{12}+4yD_{16}), -6yD_{12}]\end{aligned} \tag{B.3}$$

Similarly, for M_y, we have:

$$M_y = \mathbf{B}_{M_y}^{\mathrm{T}}\,\boldsymbol{\alpha} \tag{B.4}$$

where $\mathbf{B}_{M_y}^{\mathrm{T}}$ is:

$$\begin{aligned}\mathbf{B}_{M_y}^{\mathrm{T}} = [&-2D_{12}, -2D_{26}, -2D_{22}, -6xD_{12}, -(2yD_{12}+4xD_{26}),\\ &-(2xD_{22}+4yD_{26}), -6yD_{22}]\end{aligned} \tag{B.5}$$

For M_{xy}, we can obtain:

$$M_{xy} = \mathbf{B}_{M_{xy}}^{\mathrm{T}}\,\boldsymbol{\alpha} \tag{B.6}$$

where the matrix $\mathbf{B}_{M_{xy}}^{\mathrm{T}}$ is:

$$\begin{aligned}\mathbf{B}_{M_{xy}}^{\mathrm{T}} = [&-2D_{16}, -2D_{66}, -2D_{26}, -6xD_{16}, -(4xD_{66}+2yD_{16}),\\ &-(4yD_{66}+2xD_{26}), -6yD_{26}]\end{aligned} \tag{B.7}$$

From Eq. (2), we can calculate the derivative of the moment:

$$\begin{aligned}\frac{\partial M_x}{\partial x} &= -D_{11}\frac{\partial^3 w}{\partial x^3} - D_{12}\frac{\partial^3 w}{\partial x\partial y^2} - 2D_{16}\frac{\partial^3 w}{\partial x^2\partial y}\\ \frac{\partial M_x}{\partial y} &= -D_{11}\frac{\partial^3 w}{\partial x^2\partial y} - D_{12}\frac{\partial^3 w}{\partial y^3} - 2D_{16}\frac{\partial^3 w}{\partial x\partial y^2}\\ \frac{\partial M_y}{\partial x} &= -D_{12}\frac{\partial^3 w}{\partial x^3} - D_{22}\frac{\partial^3 w}{\partial x\partial y^2} - 2D_{26}\frac{\partial^3 w}{\partial x^2\partial y}\\ \frac{\partial M_y}{\partial y} &= -D_{12}\frac{\partial^3 w}{\partial x^2\partial y} - D_{22}\frac{\partial^3 w}{\partial y^3} - 2D_{26}\frac{\partial^3 w}{\partial x\partial y^2}\\ \frac{\partial M_{xy}}{\partial x} &= -D_{16}\frac{\partial^3 w}{\partial x^3} - D_{26}\frac{\partial^3 w}{\partial x\partial y^2} - 2D_{66}\frac{\partial^3 w}{\partial x^2\partial y}\\ \frac{\partial M_{xy}}{\partial y} &= -D_{16}\frac{\partial^3 w}{\partial x^2\partial y} - D_{26}\frac{\partial^3 w}{\partial y^3} - 2D_{66}\frac{\partial^3 w}{\partial x\partial y^2}\end{aligned} \tag{B.8}$$

Using Eq. (4), we calculate M_n for node 1 and node 2 on the side 1-2 as:

$$M_n^{12} = \cos^2\gamma_{12}\mathbf{B}_{M_x^1}^{\mathrm{T}}\boldsymbol{\alpha} + \sin^2\gamma_{12}\mathbf{B}_{M_y^1}^{\mathrm{T}}\boldsymbol{\alpha} + \sin 2\gamma_{12}\mathbf{B}_{M_{xy}^1}^{\mathrm{T}}\,\boldsymbol{\alpha} \tag{B.9}$$

$$M_n^{21} = \cos^2\gamma_{12}\mathbf{B}_{M_x^2}^{\mathrm{T}}\boldsymbol{\alpha} + \sin^2\gamma_{12}\mathbf{B}_{M_y^2}^{\mathrm{T}}\boldsymbol{\alpha} + \sin 2\gamma_{12}\mathbf{B}_{M_{xy}^2}^{\mathrm{T}}\,\boldsymbol{\alpha} \tag{B.10}$$

where $\mathbf{B}_{M_x^j}^{\mathrm{T}}$ means Eq. (B.3) evaluated at the coordinates of node j and $\mathbf{B}_{M_y^j}^{\mathrm{T}}$ means Eq. (B.5) evaluated at the coordinates of node j, respectively. And the corresponding $\mathbf{B}$ matrix is:

$$\mathbf{B}_{M_n^{12}}^{\mathrm{T}} = \cos^2\gamma_{12}\mathbf{B}_{M_x^1}^{\mathrm{T}} + \sin^2\gamma_{12}\mathbf{B}_{M_y^1}^{\mathrm{T}} + \sin 2\gamma_{12}\mathbf{B}_{M_{xy}^1}^{\mathrm{T}} \tag{B.11}$$

$$\mathbf{B}_{M_n^{21}}^{\mathrm{T}} = \cos^2\gamma_{12}\mathbf{B}_{M_x^2}^{\mathrm{T}} + \sin^2\gamma_{12}\mathbf{B}_{M_y^2}^{\mathrm{T}} + \sin 2\gamma_{12}\mathbf{B}_{M_{xy}^2}^{\mathrm{T}} \tag{B.12}$$

Similarly, M_n for the side 2-3 is:

$$M_n^{23} = \cos^2\gamma_{23}\mathbf{B}_{M_x^2}^{\mathrm{T}}\boldsymbol{\alpha} + \sin^2\gamma_{23}\mathbf{B}_{M_y^2}^{\mathrm{T}}\boldsymbol{\alpha} + \sin 2\gamma_{23}\mathbf{B}_{M_{xy}^2}^{\mathrm{T}}\,\boldsymbol{\alpha} \tag{B.13}$$

$$M_n^{32} = \cos^2\gamma_{23}\mathbf{B}_{M_x^3}^{\mathrm{T}}\boldsymbol{\alpha} + \sin^2\gamma_{23}\mathbf{B}_{M_y^3}^{\mathrm{T}}\boldsymbol{\alpha} + \sin 2\gamma_{23}\mathbf{B}_{M_{xy}^3}^{\mathrm{T}}\,\boldsymbol{\alpha} \tag{B.14}$$

And the corresponding $\mathbf{B}$ matrix is:

$$\mathbf{B}_{M_n^{23}}^{\mathrm{T}} = \cos^2\gamma_{23}\mathbf{B}_{M_x^2}^{\mathrm{T}} + \sin^2\gamma_{23}\mathbf{B}_{M_y^2}^{\mathrm{T}} + \sin 2\gamma_{23}\mathbf{B}_{M_{xy}^2}^{\mathrm{T}} \tag{B.15}$$

$$\mathbf{B}_{M_n^{32}}^{\mathrm{T}} = \cos^2\gamma_{23}\mathbf{B}_{M_x^3}^{\mathrm{T}} + \sin^2\gamma_{23}\mathbf{B}_{M_y^3}^{\mathrm{T}} + \sin 2\gamma_{23}\mathbf{B}_{M_{xy}^3}^{\mathrm{T}} \tag{B.16}$$

Finally, M_n for the side 3-1 is:

$$M_n^{31} = \cos^2\gamma_{31}\mathbf{B}_{M_x^3}^{\mathrm{T}}\boldsymbol{\alpha} + \sin^2\gamma_{31}\mathbf{B}_{M_y^3}^{\mathrm{T}}\boldsymbol{\alpha} + \sin 2\gamma_{31}\mathbf{B}_{M_{xy}^3}^{\mathrm{T}}\,\boldsymbol{\alpha} \tag{B.17}$$

$$M_n^{13} = \cos^2\gamma_{31}\mathbf{B}^{\mathrm{T}}_{M_x^1}\boldsymbol{\alpha} + \sin^2\gamma_{31}\mathbf{B}^{\mathrm{T}}_{M_y^1}\boldsymbol{\alpha} + \sin 2\gamma_{31}\mathbf{B}^{\mathrm{T}}_{M_{xy}^1}\boldsymbol{\alpha} \tag{B.18}$$

And the corresponding $\mathbf{B}$ matrix is:

$$\mathbf{B}^{\mathrm{T}}_{M_n^{31}} = \cos^2\gamma_{31}\mathbf{B}^{\mathrm{T}}_{M_x^3} + \sin^2\gamma_{31}\mathbf{B}^{\mathrm{T}}_{M_y^3} + \sin 2\gamma_{31}\mathbf{B}^{\mathrm{T}}_{M_{xy}^3} \tag{B.19}$$

$$\mathbf{B}^{\mathrm{T}}_{M_n^{13}} = \cos^2\gamma_{31}\mathbf{B}^{\mathrm{T}}_{M_x^1} + \sin^2\gamma_{31}\mathbf{B}^{\mathrm{T}}_{M_y^1} + \sin 2\gamma_{31}\mathbf{B}^{\mathrm{T}}_{M_{xy}^1} \tag{B.20}$$

Before calculating R_N, we need to calculate M_{ns} at first as shown in Eq. (11). For node 1:

$$M_{ns}^{12} = \left[\frac{1}{2}\left(\mathbf{B}^{\mathrm{T}}_{M_y^1} - \mathbf{B}^{\mathrm{T}}_{M_x^1}\right)\sin 2\gamma_{12} + \mathbf{B}^{\mathrm{T}}_{M_{xy}^1}\cos 2\gamma_{12}\right]\boldsymbol{\alpha} \tag{B.21}$$

$$M_{ns}^{13} = \left[\frac{1}{2}\left(\mathbf{B}^{\mathrm{T}}_{M_y^1} - \mathbf{B}^{\mathrm{T}}_{M_x^1}\right)\sin 2\gamma_{31} + \mathbf{B}^{\mathrm{T}}_{M_{xy}^1}\cos 2\gamma_{31}\right]\boldsymbol{\alpha} \tag{B.22}$$

Thus, plugging the above two terms into Eq. (11), R_1 is:

$$\begin{aligned} R_1 &= \left[\frac{1}{2}(\sin 2\gamma_{12} - \sin 2\gamma_{31})\left(\mathbf{B}^{\mathrm{T}}_{M_y^1} - \mathbf{B}^{\mathrm{T}}_{M_x^1}\right) + (\cos 2\gamma_{12} - \cos 2\gamma_{31})\mathbf{B}^{\mathrm{T}}_{M_{xy}^1}\right]\boldsymbol{\alpha} \\ &= \mathbf{B}_{R_1}\boldsymbol{\alpha} \end{aligned} \tag{B.23}$$

where the matrix $\mathbf{B}_{R_1}$ is:

$$\mathbf{B}^{\mathrm{T}}_{R_1} = \frac{1}{2}\left(\sin 2\gamma_{12} - \sin 2\gamma_{31}\right)\left(\mathbf{B}^{\mathrm{T}}_{M_y^1} - \mathbf{B}^{\mathrm{T}}_{M_x^1}\right) + (\cos 2\gamma_{12} - \cos 2\gamma_{31})\mathbf{B}^{\mathrm{T}}_{M_{xy}^1} \tag{B.24}$$

Similarly, the matrix $\mathbf{B}_{R_2}$ related to the node 2:

$$\mathbf{B}^{\mathrm{T}}_{R_2} = \frac{1}{2}\left(\sin 2\gamma_{23} - \sin 2\gamma_{12}\right)\left(\mathbf{B}^{\mathrm{T}}_{M_y^2} - \mathbf{B}^{\mathrm{T}}_{M_x^2}\right) + (\cos 2\gamma_{23} - \cos 2\gamma_{12})\mathbf{B}^{\mathrm{T}}_{M_{xy}^2} \tag{B.25}$$

At last, the matrix $\mathbf{B}_{R_3}$:

$$\mathbf{B}^{\mathrm{T}}_{R_3} = \frac{1}{2}\left(\sin 2\gamma_{31} - \sin 2\gamma_{23}\right)\left(\mathbf{B}^{\mathrm{T}}_{M_y^3} - \mathbf{B}^{\mathrm{T}}_{M_x^3}\right) + (\cos 2\gamma_{31} - \cos 2\gamma_{23})\mathbf{B}^{\mathrm{T}}_{M_{xy}^3} \tag{B.26}$$

In order to simplify the writing of the above formula, we define the following notations:

$$\begin{aligned} \overline{S}_1 &= \sin 2\gamma_{12} - \sin 2\gamma_{31}, \quad \overline{C}_1 = \cos 2\gamma_{12} - \cos 2\gamma_{31} \\ \overline{S}_2 &= \sin 2\gamma_{23} - \sin 2\gamma_{12}, \quad \overline{C}_2 = \cos 2\gamma_{23} - \cos 2\gamma_{12} \\ \overline{S}_3 &= \sin 2\gamma_{31} - \sin 2\gamma_{23}, \quad \overline{C}_3 = \cos 2\gamma_{31} - \cos 2\gamma_{23} \end{aligned} \tag{B.27}$$

The matrix $\mathbf{B}^{\mathrm{T}}_R$ in Eq. (B.24), (B.25) and (B.26) can be rewritten as:

$$\begin{aligned} \mathbf{B}^{\mathrm{T}}_{R_1} &= \frac{1}{2}\overline{S}_1\left(\mathbf{B}^{\mathrm{T}}_{M_y^1} - \mathbf{B}^{\mathrm{T}}_{M_x^1}\right) + \overline{C}_1\mathbf{B}^{\mathrm{T}}_{M_{xy}^1} \\ \mathbf{B}^{\mathrm{T}}_{R_2} &= \frac{1}{2}\overline{S}_2\left(\mathbf{B}^{\mathrm{T}}_{M_y^2} - \mathbf{B}^{\mathrm{T}}_{M_x^2}\right) + \overline{C}_2\mathbf{B}^{\mathrm{T}}_{M_{xy}^2} \\ \mathbf{B}^{\mathrm{T}}_{R_3} &= \frac{1}{2}\overline{S}_3\left(\mathbf{B}^{\mathrm{T}}_{M_y^3} - \mathbf{B}^{\mathrm{T}}_{M_x^3}\right) + \overline{C}_3\mathbf{B}^{\mathrm{T}}_{M_{xy}^3} \end{aligned} \tag{B.28}$$

Next, we calculate V_n according to Eqs. (5) to (8). Plugging Eqs. (7) and (8) into (5), we get:

$$V_n = \frac{\partial M_n}{\partial n} + 2\frac{\partial M_{ns}}{\partial s} \tag{B.29}$$

Plugging Eq. (12) into Eq. (B.29), we get:

$$V_n = \cos\gamma\frac{\partial M_n}{\partial x} + \sin\gamma\frac{\partial M_n}{\partial y} - 2\sin\gamma\frac{\partial M_{ns}}{\partial x} + 2\cos\gamma\frac{\partial M_{ns}}{\partial y} \tag{B.30}$$

The terms on the RHS above require eventually the evaluation of $\frac{\partial M_n}{\partial x}$, $\frac{\partial M_n}{\partial y}$, $\frac{\partial M_{ns}}{\partial x}$, and $\frac{\partial M_{ns}}{\partial y}$.

For V_n^{12} item, the derivation from Eq. (B.9) is:

$$\frac{\partial M_n^{12}}{\partial x} = \cos^2\gamma_{12}\frac{\partial \mathbf{B}^{\mathrm{T}}_{M_x^1}}{\partial x}\boldsymbol{\alpha} + \sin^2\gamma_{12}\frac{\partial \mathbf{B}^{\mathrm{T}}_{M_y^1}}{\partial x}\boldsymbol{\alpha} + \sin 2\gamma_{12}\frac{\partial \mathbf{B}^{\mathrm{T}}_{M_{xy}^1}}{\partial x}\boldsymbol{\alpha} \tag{B.31}$$

$$\frac{\partial M_n^{12}}{\partial y} = \cos^2\gamma_{12}\frac{\partial \mathbf{B}^{\mathrm{T}}_{M_x^1}}{\partial y}\boldsymbol{\alpha} + \sin^2\gamma_{12}\frac{\partial \mathbf{B}^{\mathrm{T}}_{M_y^1}}{\partial y}\boldsymbol{\alpha} + \sin 2\gamma_{12}\frac{\partial \mathbf{B}^{\mathrm{T}}_{M_{xy}^1}}{\partial y}\boldsymbol{\alpha} \tag{B.32}$$

where

$$\frac{\partial \mathbf{B}^{\mathrm{T}}_{M_x^1}}{\partial x} = \left[0,\ 0,\ 0,\ -6D_{11},\ -4D_{16},\ -2D_{12},\ 0\right] \tag{B.33}$$

$$\frac{\partial \mathbf{B}^{\mathrm{T}}_{M_y^1}}{\partial x} = \left[0,\ 0,\ 0,\ -6D_{12},\ -4D_{26},\ -2D_{22},\ 0\right] \tag{B.34}$$

$$\frac{\partial \mathbf{B}^{\mathrm{T}}_{M_{xy}^1}}{\partial x} = \left[0,\ 0,\ 0,\ -6D_{16},\ -4D_{66},\ -2D_{26},\ 0\right] \tag{B.35}$$

And

$$\frac{\partial \mathbf{B}^{\mathrm{T}}_{M_x^1}}{\partial y} = \left[0,\ 0,\ 0,\ 0,\ -2D_{11},\ -4D_{16},\ -6D_{12}\right] \tag{B.36}$$

$$\frac{\partial \mathbf{B}^{\mathrm{T}}_{M_y^1}}{\partial y} = \left[0,\ 0,\ 0,\ 0,\ -2D_{12},\ -4D_{26},\ -6D_{22}\right] \tag{B.37}$$

$$\frac{\partial \mathbf{B}^{\mathrm{T}}_{M_{xy}^1}}{\partial y} = \left[0,\ 0,\ 0,\ 0,\ -2D_{16},\ -4D_{66},\ -6D_{26}\right] \tag{B.38}$$

Thus, the matrix $\mathbf{B}^{\mathrm{T}}_{M_{n,x}^{12}}$ and $\mathbf{B}^{\mathrm{T}}_{M_{n,y}^{12}}$ are:

$$\mathbf{B}^{\mathrm{T}}_{M_{n,x}^{12}} = \cos^2\gamma_{12}\frac{\partial \mathbf{B}^{\mathrm{T}}_{M_x^1}}{\partial x} + \sin^2\gamma_{12}\frac{\partial \mathbf{B}^{\mathrm{T}}_{M_y^1}}{\partial x} + \sin 2\gamma_{12}\frac{\partial \mathbf{B}^{\mathrm{T}}_{M_{xy}^1}}{\partial x} \tag{B.39}$$

$$\mathbf{B}^{\mathrm{T}}_{M_{n,y}^{12}} = \cos^2\gamma_{12}\frac{\partial \mathbf{B}^{\mathrm{T}}_{M_x^1}}{\partial y} + \sin^2\gamma_{12}\frac{\partial \mathbf{B}^{\mathrm{T}}_{M_y^1}}{\partial y} + \sin 2\gamma_{12}\frac{\partial \mathbf{B}^{\mathrm{T}}_{M_{xy}^1}}{\partial y} \tag{B.40}$$

Using Eq. (7), the derivative of moment M_{ns} on side 1-2 is:

$$\frac{\partial M_{ns}^{12}}{\partial x} = \left[\frac{1}{2}\left(\frac{\partial \mathbf{B}^{\mathrm{T}}_{M_y^1}}{\partial x} - \frac{\partial \mathbf{B}^{\mathrm{T}}_{M_x^1}}{\partial x}\right)\sin 2\gamma_{12} + \frac{\partial \mathbf{B}^{\mathrm{T}}_{M_{xy}^1}}{\partial x}\cos 2\gamma_{12}\right]\boldsymbol{\alpha} \tag{B.41}$$

$$\frac{\partial M_{ns}^{12}}{\partial y} = \left[\frac{1}{2}\left(\frac{\partial \mathbf{B}^{\mathrm{T}}_{M_y^1}}{\partial y} - \frac{\partial \mathbf{B}^{\mathrm{T}}_{M_x^1}}{\partial y}\right)\sin 2\gamma_{12} + \frac{\partial \mathbf{B}^{\mathrm{T}}_{M_{xy}^1}}{\partial y}\cos 2\gamma_{12}\right]\boldsymbol{\alpha} \tag{B.42}$$

Thus, the matrices $\mathbf{B}^{\mathrm{T}}_{M_{ns,x}^{12}}$ and $\mathbf{B}^{\mathrm{T}}_{M_{ns,y}^{12}}$ are:

$$\mathbf{B}^{\mathrm{T}}_{M_{ns,x}^{12}} = \frac{1}{2}\sin 2\gamma_{12}\left(\frac{\partial \mathbf{B}^{\mathrm{T}}_{M_y^1}}{\partial x} - \frac{\partial \mathbf{B}^{\mathrm{T}}_{M_x^1}}{\partial x}\right) + \cos 2\gamma_{12}\frac{\partial \mathbf{B}^{\mathrm{T}}_{M_{xy}^1}}{\partial x} \tag{B.43}$$

$$\mathbf{B}^{\mathrm{T}}_{M_{ns,y}^{12}} = \frac{1}{2}\sin 2\gamma_{12}\left(\frac{\partial \mathbf{B}^{\mathrm{T}}_{M_y^1}}{\partial y} - \frac{\partial \mathbf{B}^{\mathrm{T}}_{M_x^1}}{\partial y}\right) + \cos 2\gamma_{12}\frac{\partial \mathbf{B}^{\mathrm{T}}_{M_{xy}^1}}{\partial y} \tag{B.44}$$

Finally, using Eq. (B.30), $\mathbf{B}$ matrix for the Kirchhoff shear force V_n on side 1-2 is:

$$\mathbf{B}^{\mathrm{T}}_{V_n^{12}} = \cos\gamma_{12}\mathbf{B}^{\mathrm{T}}_{M_{n,x}^{12}} + \sin\gamma_{12}\mathbf{B}^{\mathrm{T}}_{M_{n,y}^{12}} - 2\sin\gamma_{12}\mathbf{B}^{\mathrm{T}}_{M_{ns,x}^{12}} + 2\cos\gamma_{12}\mathbf{B}^{\mathrm{T}}_{M_{ns,y}^{12}} \tag{B.45}$$

Similarly, $\mathbf{B}_{V_n}$ matrix on side 2-3 is:

$$\mathbf{B}^{\mathrm{T}}_{M_{n,x}^{23}} = \cos^2\gamma_{23}\frac{\partial \mathbf{B}^{\mathrm{T}}_{M_x^2}}{\partial x} + \sin^2\gamma_{23}\frac{\partial \mathbf{B}^{\mathrm{T}}_{M_y^2}}{\partial x} + \sin 2\gamma_{23}\frac{\partial \mathbf{B}^{\mathrm{T}}_{M_{xy}^1}}{\partial x} \tag{B.46}$$

$$\mathbf{B}^{\mathrm{T}}_{M_{n,y}^{23}} = \cos^2\gamma_{23}\frac{\partial \mathbf{B}^{\mathrm{T}}_{M_x^2}}{\partial y} + \sin^2\gamma_{23}\frac{\partial \mathbf{B}^{\mathrm{T}}_{M_y^2}}{\partial y} + \sin 2\gamma_{23}\frac{\partial \mathbf{B}^{\mathrm{T}}_{M_{xy}^2}}{\partial y} \tag{B.47}$$

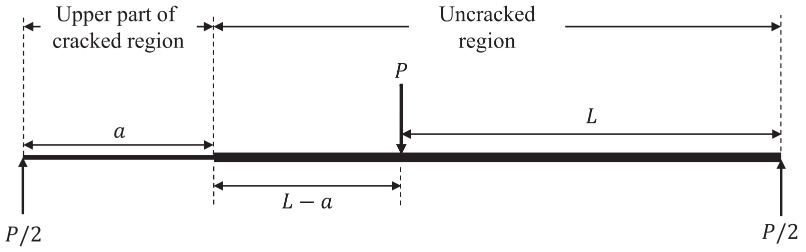

Fig. C.1. Analytical solution of SLB model.

and

$$\mathbf{B}^{\mathrm{T}}_{M^{23}_{ns,x}} = \frac{1}{2}\sin 2\gamma_{23}\left(\frac{\partial \mathbf{B}^{\mathrm{T}}_{M^2_y}}{\partial x} - \frac{\partial \mathbf{B}^{\mathrm{T}}_{M^2_x}}{\partial x}\right) + \cos 2\gamma_{23}\frac{\partial \mathbf{B}^{\mathrm{T}}_{M^2_{xy}}}{\partial x} \tag{B.48}$$

$$\mathbf{B}^{\mathrm{T}}_{M^{23}_{ns,y}} = \frac{1}{2}\sin 2\gamma_{23}\left(\frac{\partial \mathbf{B}^{\mathrm{T}}_{M^2_y}}{\partial y} - \frac{\partial \mathbf{B}^{\mathrm{T}}_{M^2_x}}{\partial y}\right) + \cos 2\gamma_{23}\frac{\partial \mathbf{B}^{\mathrm{T}}_{M^2_{xy}}}{\partial y} \tag{B.49}$$

The **B** matrix for V^{23}_n is:

$$\mathbf{B}^{\mathrm{T}}_{V^{23}_n} = \cos\gamma_{23}\mathbf{B}^{\mathrm{T}}_{M^{23}_{n,x}} + \sin\gamma_{23}\mathbf{B}^{\mathrm{T}}_{M^{23}_{n,y}} - 2\sin\gamma_{23}\mathbf{B}^{\mathrm{T}}_{M^{23}_{ns,x}} + 2\cos\gamma_{23}\mathbf{B}^{\mathrm{T}}_{M^{23}_{ns,y}} \tag{B.50}$$

On side 3-1:

$$\mathbf{B}^{\mathrm{T}}_{M^{31}_{n,x}} = \cos^2\gamma_{31}\frac{\partial \mathbf{B}^{\mathrm{T}}_{M^3_x}}{\partial x} + \sin^2\gamma_{31}\frac{\partial \mathbf{B}^{\mathrm{T}}_{M^3_y}}{\partial x} + \sin 2\gamma_{31}\frac{\partial \mathbf{B}^{\mathrm{T}}_{M^3_{xy}}}{\partial x} \tag{B.51}$$

$$\mathbf{B}^{\mathrm{T}}_{M^{31}_{n,y}} = \cos^2\gamma_{31}\frac{\partial \mathbf{B}^{\mathrm{T}}_{M^3_x}}{\partial y} + \sin^2\gamma_{31}\frac{\partial \mathbf{B}^{\mathrm{T}}_{M^3_y}}{\partial y} + \sin 2\gamma_{31}\frac{\partial \mathbf{B}^{\mathrm{T}}_{M^3_{xy}}}{\partial y} \tag{B.52}$$

and

$$\mathbf{B}^{\mathrm{T}}_{M^{31}_{ns,x}} = \frac{1}{2}\sin 2\gamma_{31}\left(\frac{\partial \mathbf{B}^{\mathrm{T}}_{M^3_y}}{\partial x} - \frac{\partial \mathbf{B}^{\mathrm{T}}_{M^3_x}}{\partial x}\right) + \cos 2\gamma_{31}\frac{\partial \mathbf{B}^{\mathrm{T}}_{M^3_{xy}}}{\partial x} \tag{B.53}$$

$$\mathbf{B}^{\mathrm{T}}_{M^{31}_{ns,y}} = \frac{1}{2}\sin 2\gamma_{31}\left(\frac{\partial \mathbf{B}^{\mathrm{T}}_{M^3_y}}{\partial y} - \frac{\partial \mathbf{B}^{\mathrm{T}}_{M^3_x}}{\partial y}\right) + \cos 2\gamma_{31}\frac{\partial \mathbf{B}^{\mathrm{T}}_{M^3_{xy}}}{\partial y} \tag{B.54}$$

The **B** matrix for V^{31}_n is:

$$\mathbf{B}^{\mathrm{T}}_{V^{31}_n} = \cos\gamma_{31}\mathbf{B}^{\mathrm{T}}_{M^{31}_{n,x}} + \sin\gamma_{23}\mathbf{B}^{\mathrm{T}}_{M^{31}_{n,y}} - 2\sin\gamma_{23}\mathbf{B}^{\mathrm{T}}_{M^{31}_{ns,x}} + 2\cos\gamma_{23}\mathbf{B}^{\mathrm{T}}_{M^{31}_{ns,y}}$$

Therefore, the calculations of **B** matrices for V_n on sides 23 and 31 can be simplified through the use of the pre-calculated matrices for side 12.

Now, all the components of **B** matrix have been derived. The assembled (7×12) matrix **B** is:

$$\mathbf{B} = [\mathbf{B}_{R_1}, \mathbf{B}_{R_2}, \mathbf{B}_{R_3}, \mathbf{B}_{V^{12}_n}, \mathbf{B}_{V^{23}_n}, \mathbf{B}_{V^{31}_n}, \mathbf{B}_{M^{12}_n}, \mathbf{B}_{M^{21}_n}, \mathbf{B}_{M^{23}_n}, \mathbf{B}_{M^{32}_n}, \mathbf{B}_{M^{31}_n}, \mathbf{B}_{M^{13}_n}] \tag{B.55}$$

Appendix C. Analytical solution of SLB benchmark

Referring to Fig. C.1, the analytical load–displacement curve consists of three parts. The first part, OB, is the linear elastic stage with the initial crack length a_0. The second part comes from the curve ABC which represents the load–displacement response during delamination propagation when $a < L$ (the half length of the SLB model). When $a > L$, we can obtain the last curve DFE. The full analytical curve would then be OBFE. The derivation process of each curve is shown one by one in the following content.

When the crack length a is smaller than L, the analytical derivation of the SLB benchmark follows from the work of Davidson et al. [45]. Referring to the SLB model in Fig. 14, it is evident that the bending stiffness in the cracked region comes entirely from the part above the crack, which is midplane symmetrical. The uncracked region is midplane anti-symmetric.

The SLB model ($a < L$) is simplified into a 2D beam model, as shown in Fig. C.2. The moment–curvature relationship for the SLB problem can be expressed as:

$$M = -b\,D\,\frac{\mathrm{d}^2 w}{\mathrm{d}x^2} = b\,D\,\kappa_x \tag{C.1}$$

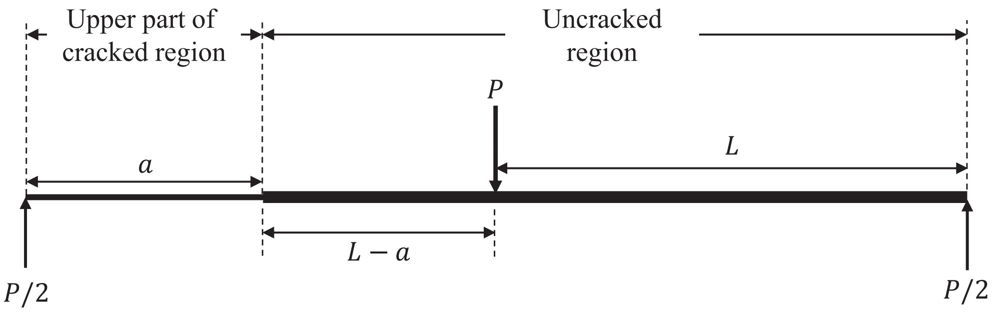

Fig. C.2. Beam model of SLB specimen ($a < L$).

where M is the moment on a face along the x-axis, b is the width of the specimen, w is the deflection along the z direction. And D is the effective bending rigidity per unit width. Because the values of D in the uncracked region and cracked regions are different, D_0 represents the effective bending rigidity of the uncracked region, and D_1 represents the effective bending rigidity of the cracked region to distinguish them.

We assume that the classical laminate theory is applicable to the SLB problem. In matrix form, the constitutive equation can be written as:

$$\begin{bmatrix} N_x \\ N_y \\ N_{xy} \\ -- \\ M_x \\ M_y \\ M_{xy} \end{bmatrix} = \begin{bmatrix} A_{11} & A_{12} & A_{16} & | & B_{11} & B_{12} & B_{16} \\ A_{12} & A_{22} & A_{26} & | & B_{12} & B_{22} & B_{26} \\ A_{16} & A_{26} & A_{66} & | & B_{16} & B_{26} & B_{66} \\ -- & -- & -- & | & -- & -- & -- \\ B_{11} & B_{12} & B_{16} & | & D_{11} & D_{12} & D_{16} \\ B_{12} & B_{22} & B_{26} & | & D_{12} & D_{22} & D_{26} \\ B_{16} & B_{26} & B_{66} & | & D_{16} & D_{26} & D_{66} \end{bmatrix} \begin{bmatrix} \varepsilon_x^0 \\ \varepsilon_y^0 \\ \gamma_{xy}^0 \\ -- \\ \kappa_x \\ \kappa_y \\ \kappa_{xy} \end{bmatrix} \tag{C.2}$$

where ε_x^0, ε_y^0, γ_{xy}^0 are the membrane strains of the neutral plane, and κ_x, κ_y, κ_{xy} are the curvatures, derived from the out-of-plane displacement w:

$$\kappa_x = -\frac{\partial^2 w}{\partial x^2}, \quad \kappa_y = -\frac{\partial^2 w}{\partial y^2}, \quad \kappa_{xy} = -\frac{\partial^2 w}{\partial x \partial y} \tag{C.3}$$

The inverted form of the constitutive relationship is:

$$\begin{bmatrix} \varepsilon_x^0 \\ \varepsilon_y^0 \\ \gamma_{xy}^0 \\ -- \\ \kappa_x \\ \kappa_y \\ \kappa_{xy} \end{bmatrix} = \begin{bmatrix} \alpha_{11} & \alpha_{12} & \alpha_{16} & | & \beta_{11} & \beta_{12} & \beta_{16} \\ \alpha_{12} & \alpha_{22} & \alpha_{26} & | & \beta_{12} & \beta_{22} & \beta_{26} \\ \alpha_{16} & \alpha_{26} & \alpha_{66} & | & \beta_{16} & \beta_{26} & \beta_{66} \\ -- & -- & -- & | & -- & -- & -- \\ \beta_{11} & \beta_{12} & \beta_{16} & | & \delta_{11} & \delta_{12} & \delta_{16} \\ \beta_{12} & \beta_{22} & \beta_{26} & | & \delta_{12} & \delta_{22} & \delta_{26} \\ \beta_{16} & \beta_{26} & \beta_{66} & | & \delta_{16} & \delta_{26} & \delta_{66} \end{bmatrix} \begin{bmatrix} N_x \\ N_y \\ N_{xy} \\ -- \\ M_x \\ M_y \\ M_{xy} \end{bmatrix} \tag{C.4}$$

If the plate constraint condition is "generalized plane stress", N_y, N_{xy}, M_y, and M_{xy} are zero. When considering $N_x = 0$, Eq. (C.4) gives:

$$D = \frac{1}{\delta_{11}} \tag{C.5}$$

For the plane strain condition ($\epsilon_y^0 = \gamma_{xy}^0 = \kappa_y = \kappa_{xy} = 0$), Eq. (C.2) gives:

$$D = D_{11} \tag{C.6}$$

The expression of strain energy is:

$$U = \int_0^{2L} \frac{M^2 \mathrm{d}x}{2bD} \tag{C.7}$$

From Fig. C.2, the boundary conditions of the SLB model can be considered similar to three-point bending. So we can get the moment along the beam as:

$$M = \begin{cases} -\dfrac{Px}{2}, & 0 \le x \le L \\ \dfrac{Px}{2} - PL, & L \le x \le 2L \end{cases} \tag{C.8}$$

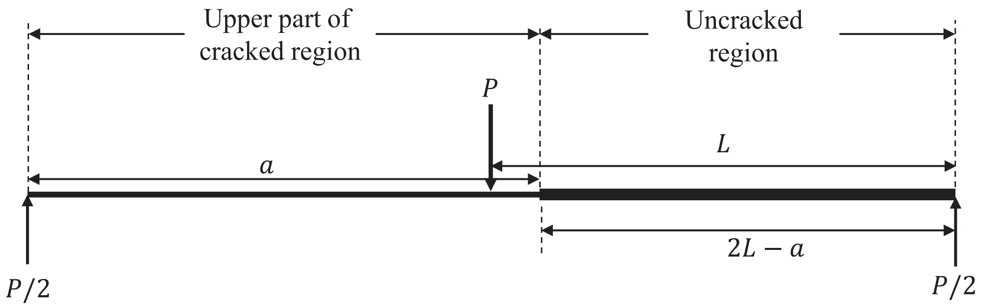

Fig. C.3. Beam model of SLB specimen ($a \geq L$).

Since the cross-section of the upper part of the cracked region ($0 \leq x \leq a$) is different from that of the uncracked region, the moment M is further divided, and the expression for strain energy is the sum of three parts:

$$U|_{(a<L)} = \int_0^a \frac{M^2 \mathrm{d}x}{2bD_1} + \int_a^{L-a} \frac{M^2 \mathrm{d}x}{2bD_0} + \int_L^{2L} \frac{M^2 \mathrm{d}x}{2bD_0} \tag{C.9}$$

Substituting Eq. (C.8) into Eq. (C.9), we can get:

$$U|_{(a<L)} = \int_0^a \frac{\left(-\frac{Px}{2}\right)^2 \mathrm{d}x}{2bD_1} + \int_a^L \frac{\left(-\frac{Px}{2}\right)^2 \mathrm{d}x}{2bD_0} + \int_L^{2L} \frac{\left(\frac{Px}{2} - PL\right)^2 \mathrm{d}x}{2bD_0} \tag{C.10}$$

Based on the expression of strain energy, the displacement δ can be calculated by Castigliano's second theorem:

$$\begin{aligned} \delta|_{(a<L)} &= \frac{\partial U|_{(a<L)}}{\partial P} = \int_0^a \frac{Px^2 \mathrm{d}x}{4bD_1} + \int_a^L \frac{Px^2 \mathrm{d}x}{4bD_0} + \int_L^{2L} \frac{\left(Px^2 - 4PLx + 4PL^2\right) \mathrm{d}x}{4bD_0} \\ &= \frac{Pa^3}{12bD_1} + \frac{2PL^3 - Pa^3}{12bD_0} \end{aligned} \tag{C.11}$$

The above equation can be used to plot the $P - \delta$ curve for a certain crack length a, which for the case of $a = a_0$ gives the first part of the analytical curve, i.e., OB. The compliance C during the elastic region is defined as the centre deflection δ divided by the centre load P:

$$C|_{(a<L)} = \frac{\delta|_{(a<L)}}{P} = \frac{2L^3 + a^3(R-1)}{12bD_0} \tag{C.12}$$

where R is the ratio of the bending rigidity of the uncracked region to that of the cracked region:

$$R = D_0/D_1 \tag{C.13}$$

The relationship between the critical energy release rate G_c and the derivative of compliance C with respect to the crack length a is:

$$G_c = \frac{P^2}{2b}\frac{\partial C}{\partial a} \tag{C.14}$$

Substituting Eq. (C.12) into Eq. (C.14), we can obtain:

$$G_c = \frac{P^2 a^2 (R-1)}{8b^2 D_0} \tag{C.15}$$

Substituting Eq. (C.12) to Eq. (C.15), the critical energy release rate G_c can also be obtained by the critical load and deflection:

$$G_c = \frac{3Pa^2\ \delta|_{(a<L)}}{2b} \frac{(R-1)}{[2L^3 + a^3(R-1)]} \tag{C.16}$$

The critical energy release rate G_c in Eq. (C.16) is the value in mixed mode. It can be calculated by:

$$G_c = G_{\mathrm{Ic}} + (G_{\mathrm{IIc}} - G_{\mathrm{Ic}})B^{\eta} \tag{C.17}$$

where G_{Ic} and G_{IIc} are the critical energy release rates in pure mode I and mode II, respectively. The mixed mode ratio B in the SLB model is 0.4 [46]. Eq. (C.15) can be used to calculate the critical load P at a certain crack length a. It can also be used to express a in terms of P for a fixed G_c, which can be plugged into Eq. (C.16) to obtain the relationship between δ and P for a fixed G_c for the case of $a < L$, hence giving the curve ABC.

When the crack length a is greater than or equal to L, the analytical derivation of the SLB benchmark can follow the same derivation process as above. The SLB model ($a \geq L$) is simplified in Fig. C.3. Based on Fig. C.3, the expression for strain energy is rewritten as:

$$U|_{(a\geq L)} = \int_0^L \frac{M^2 \mathrm{d}x}{2bD_1} + \int_L^a \frac{M^2 \mathrm{d}x}{2bD_1} + \int_a^{2L} \frac{M^2 \mathrm{d}x}{2bD_0} \tag{C.18}$$

Since the boundary conditions have not changed, the expression of the moment is consistent with Eq. (C.8). Substituting Eq. (C.8) into Eq. (C.18), we can obtain:

$$\begin{aligned} U|_{(a\geq L)} = &\int_0^L \frac{P^2x^2 \mathrm{d}x}{8bD_1} + \int_L^a \frac{\left(P^2x^2 - 4P^2Lx + 4P^2L^2\right)\mathrm{d}x}{8bD_1} \\ &+ \int_a^{2L} \frac{\left(P^2x^2 - 4P^2Lx + 4P^2L^2\right)\mathrm{d}x}{8bD_0} \end{aligned} \tag{C.19}$$

The displacement δ at the middle can also be found by Castigliano's second theorem:

$$\delta|_{(a\geq L)} = -\frac{PL^3}{2bD_1} + \frac{Pa^3 - 6PLa^2 + 12PL^2a}{12bD_1} + \frac{8PL^3}{12bD_0} - \frac{Pa^3 - 6PLa^2 + 12PL^2a}{12bD_0} \tag{C.20}$$

Introducing ratio R in Eq. (C.13), the above equation can be rewritten as:

$$\delta|_{(a\geq L)} = -\frac{(6R-8)PL^3}{12bD_0} + \frac{(R-1)(Pa^3 - 6PLa^2 + 12PL^2a)}{12bD_0} \tag{C.21}$$

The expression of compliance C under the condition $a \geq L$ is:

$$C|_{(a\geq L)} = \frac{\delta|_{(a\geq L)}}{P} = -\frac{(6R-8)L^3}{12bD_0} + \frac{(R-1)(a^3 - 6La^2 + 12L^2a)}{12bD_0} \tag{C.22}$$

Substituting Eq. (C.22) into Eq. (C.14), we have:

$$G_c = \frac{P^2(R-1)(3a^2 - 12aL + 12L^2)}{24b^2D_0} \tag{C.23}$$

where G_c is the critical energy release rate given by Eq. (C.17). Using Eqs. (C.21) and (C.23), one can then vary a to plot the third part of the analytical curve DE.

Data availability

Data will be made available on request.

References

[1] Barenblatt GI. The mathematical theory of equilibrium cracks in brittle fracture. Adv Appl Mech 1962;7:55–129.
[2] Dugdale DS. Yielding of steel sheets containing slits. J Mech Phys Solids 1960;8(2):100–4.
[3] Qiu Y, Crisfield MA, Alfano G. An interface element formulation for the simulation of delamination with buckling. Eng Fract Mech 2001;68(16):1755–76.
[4] Yang Q, Cox B. Cohesive models for damage evolution in laminated composites. Int J Fract 2005;133(2):107–37.
[5] Camanho PP, Dávila CG. Mixed-mode decohesion finite elements for the simulation of delamination in composite materials. NASA Technical Reports 211737, 2002.
[6] Moës N, Belytschko T. Extended finite element method for cohesive crack growth. Eng Fract Mech 2002;69(7):813–33.
[7] Xu X-P, Needleman A. Void nucleation by inclusion debonding in a crystal matrix. Modelling Simul Mater Sci Eng 1993;1(2):111.
[8] Turon A, Davila CG, Camanho PP, Costa J. An engineering solution for mesh size effects in the simulation of delamination using cohesive zone models. Eng Fract Mech 2007;74(10):1665–82.
[9] Pirondi A, Giuliese G, Moroni F, Bernasconi A, Jamil A. Comparative study of cohesive zone and virtual crack closure techniques for three-dimensional fatigue debonding. J Adhes 2014;90(5–6):457–81.
[10] Chen J, Crisfield M, Kinloch AJ, Busso EP, Matthews FL, Qiu Y. Predicting progressive delamination of composite material specimens via interface elements. Mech Compos Mater Struct 1999;6(4):301–17.
[11] Rafiee R, Sotoudeh S. A hysteresis cohesive approach for predicting mixed-mode delamination onset of composite laminates under cyclic loading: Part i, model development. Compos Struct 2021;277:114667.
[12] Rafiee R, Sotoudeh S. A hysteresis cohesive approach for predicting mixed-mode delamination onset of composite laminates under cyclic loading: Part II, numerical and experimental analyses. Compos Struct 2021;277:114668.
[13] Falk ML, Needleman A, Rice JR. A critical evaluation of cohesive zone models of dynamic fracture. Le J Phys IV 2001;11(PR5):Pr5–43.
[14] Kubair DV, Geubelle PH. Comparative analysis of extrinsic and intrinsic cohesive models of dynamic fracture. Int J Solids Struct 2003;40(15):3853–68.
[15] Seagraves A, Radovitzky R. Advances in cohesive zone modeling of dynamic fracture. In: Dynamic failure of materials and structures. Springer; 2009, p. 349–405.
[16] Pandolfi A, Ortiz M. An efficient adaptive procedure for three-dimensional fragmentation simulations. Eng Comput 2002;18(2):148–59.
[17] Mergheim J, Kuhl E, Steinmann P. A hybrid discontinuous Galerkin/interface method for the computational modelling of failure. Commun Numer Methods Eng 2004;20(7):511–9.
[18] Lorentz E. A mixed interface finite element for cohesive zone models. Comput Methods Appl Mech Engrg 2008;198(2):302–17.
[19] Harper PW, Hallett SR. Cohesive zone length in numerical simulations of composite delamination. Eng Fract Mech 2008;75(16):4774–92.
[20] Lu X, Ridha M, Chen B, Tan V, Tay T. On cohesive element parameters and delamination modelling. Eng Fract Mech 2019;206:278–96.
[21] Yang Q, Fang X, Shi J, Lua J. An improved cohesive element for shell delamination analyses. Internat J Numer Methods Engrg 2010;83(5):611–41.

[22] Do B, Liu W, Yang Q, Su X. Improved cohesive stress integration schemes for cohesive zone elements. Eng Fract Mech 2013;107:14–28.

[23] Russo R, Chen B. Overcoming the cohesive zone limit in composites delamination: modeling with slender structural elements and higher-order adaptive integration. Internat J Numer Methods Engrg 2020;121(24):5511–45.

[24] Guiamatsia I, Ankersen J, Davies G, Iannucci L. Decohesion finite element with enriched basis functions for delamination. Compos Sci Technol 2009;69(15–16):2616–24.

[25] Guiamatsia I, Davies G, Ankersen J, Iannucci L. A framework for cohesive element enrichment. Compos Struct 2010;92(2):454–9.

[26] Guiamatsia I, Ankersen J, Iannucci L. A study of mixed-mode composite delamination using enriched interface elements. Aeronaut J 2013;117(1195):959–67.

[27] Samimi M, Van Dommelen J, Geers M. An enriched cohesive zone model for delamination in brittle interfaces. Internat J Numer Methods Engrg 2009;80(5):609–30.

[28] Samimi M, Van Dommelen J, Geers M. A self-adaptive finite element approach for simulation of mixed-mode delamination using cohesive zone models. Eng Fract Mech 2011;78(10):2202–19.

[29] Samimi M, Van Dommelen J, Geers M. A three-dimensional self-adaptive cohesive zone model for interfacial delamination. Comput Methods Appl Mech Engrg 2011;200(49–52):3540–53.

[30] Van der Meer F, Moës N, Sluys LJ. A level set model for delamination–modeling crack growth without cohesive zone or stress singularity. Eng Fract Mech 2012;79:191–212.

[31] Lu X, Chen B-Y, Tan VB, Tay T-E. Adaptive floating node method for modelling cohesive fracture of composite materials. Eng Fract Mech 2018;194:240–61.

[32] Chen B, Pinho S, De Carvalho N, Baiz P, Tay T. A floating node method for the modelling of discontinuities in composites. Eng Fract Mech 2014;127:104–34.

[33] Álvarez D, Blackman B, Guild F, Kinloch A. Mode I fracture in adhesively-bonded joints: A mesh-size independent modelling approach using cohesive elements. Eng Fract Mech 2014;115:73–95.

[34] Mukhopadhyay S, Bhatia S. Accurate coarse mesh simulation of delamination in composites using a novel hp-adaptive cohesive element. J Compos Mater 2023;57(13):2201–18.

[35] Daniel PM, Främby J, Fagerström M, Maimí P. An efficient ERR-cohesive method for the modelling of delamination propagation with large elements. Compos Part A: Appl Sci Manuf 2023;167:107423.

[36] Tosti Balducci G, Chen B. Overcoming the cohesive zone limit in the modelling of composites delamination with TUBA cohesive elements. 2024, arXiv preprint arXiv:2403.09895.

[37] Bell K. A refined triangular plate bending finite element. Internat J Numer Methods Engrg 1969;1(1):101–22.

[38] Dávila CG, Camanho PMPRdC, Turon Travesa A. Cohesive Elements for Shells. ©NASA TP Technical Reports 2007, National Aeronautics and Space Administration; 2007, Núm. 214869.

[39] Bazilevs Y, Pigazzini M, Ellison A, Kim H. A new multi-layer approach for progressive damage simulation in composite laminates based on isogeometric analysis and Kirchhoff–Love shells. Part I: basic theory and modeling of delamination and transverse shear. Comput Mech 2018;62:563–85.

[40] Allman D. A simple cubic displacement element for plate bending. Internat J Numer Methods Engrg 1976;10(2):263–81.

[41] Przemieniecki JS. Theory of matrix structural analysis. Courier Corporation; 1985.

[42] Turon A, Camanho PP, Costa J, Dávila C. A damage model for the simulation of delamination in advanced composites under variable-mode loading. Mech Mater 2006;38(11):1072–89.

[43] Turon A, Camanho P, Costa J, Renart J. Accurate simulation of delamination growth under mixed-mode loading using cohesive elements: Definition of interlaminar strengths and elastic stiffness. Compos Struct 2010;92(8):1857–64.

[44] Cowper G. Gaussian quadrature formulas for triangles. Internat J Numer Methods Engrg 1973;7(3):405–8.

[45] Davidson B, Krüger R, König M. Three-dimensional analysis of center-delaminated unidirectional and multidirectional single-leg bending specimens. Compos Sci Technol 1995;54(4):385–94.

[46] Krueger R. A summary of benchmark examples to assess the performance of quasi-static delamination propagation prediction capabilities in finite element codes. J Compos Mater 2015;49(26):3297–316.

[47] Williams J. The fracture mechanics of delamination tests. J Strain Anal Eng Des 1989;24(4):207–14.

[48] ASTM D5528 /D5528M-21, Standard test method for mode I interlaminar fracture toughness of unidirectional fiber-reinforced polymer matrix composites. West Conshohocken, PA: ASTM-International; 2007.

[49] ASTM D6671 /D6671M-22, Standard test method for mixed mode I -mode II interlaminar fracture toughness of unidirectional fiber reinforced polymer matrix composites. West Conshohocken, PA: ASTM-International; 2022.

[50] Carreras L, Renart J, Turon A, Costa J, Bak BLV, Lindgaard E, de la Escalera FM, Essa Y. A benchmark test for validating 3D simulation methods for delamination growth under quasi-static and fatigue loading. Compos Struct 2019;210:932–41.

[51] Carreras L, Turon A, Bak BL, Lindgaard E, Renart J, de la Escalera FM, Essa Y. A simulation method for fatigue-driven delamination in layered structures involving non-negligible fracture process zones and arbitrarily shaped crack fronts. Compos Part A: Appl Sci Manuf 2019;122:107–19.

[52] Bruyneel M, Delsemme J-P, Jetteur P, Germain F. Modeling inter-laminar failure in composite structures: illustration on an industrial case study. Appl Compos Mater 2009;16(3):149–62.

[53] Krueger R, Deobald L, Gu H. A benchmark example for delamination growth predictions based on the single leg bending specimen under fatigue loading. Adv Model Simul Eng Sci 2020;7:1–25.